Engineering the compositional architecture of core-shell upconverting lanthanide-doped nanoparticles for optimal luminescent donor in resonance energy transfer : the effects of energy migration and storage

Aleksandra Pilch-Wrobel[a‡], Agata M. Kotulska[a‡], Satu Lahtinen[b],

Tero Soukka[b*], Artur Bednarkiewicz[a*]

[a]Institute of Low Temperature and Structure Research, PAN, ul.Okolna 2, Wrocław 50-422, Poland

[b]University of Turku, Department of Life Technologies/Biotechnology, Kiinamyllynkatu 10, 20520 Turku, Finland

Corresponding authors

* E-mail: tero.soukka@utu.fi, Tel. +358 50 476 5571

* E-mail a.bednarkiewicz@intibs.pl, Tel. +48 71 3954 291

ABSTRACT

Förster Resonance Energy Transfer (FRET) between single molecule donor (***D***) and acceptor (***A***) is well understood from fundamental perspective and is widely applied in biology, biotechnology, medical diagnostics and bio-imaging. However, the reliability of molecular FRET measurements can be affected by numerous artefacts which eventually hamper quantitative and reliable analysis, mostly due to issues with the donor and acceptor molecules. Lanthanide doped upconverting nanoparticles (UCNPs) have demonstrated their suitability as alternative donor species. Nevertheless, while they solved most disadvantageous features of organic donor molecules, such as photo-bleaching, spectral cross-excitation and emission bleed-through, the fundamental understanding and practical realizations of bio-assays with UCNP donors remain challenging. Among others, the actual donor ions in individual donor UCNPs are the numerous activator ions randomly distributed in the nanoparticle at various distances to acceptors anchored on the nanoparticle surface. Further, the power dependent, complex energy transfer upconversion and energy migration between sensitizing and activating lanthanide ions within UCNPs complicate the decay based analysis of ***D***-***A*** interaction. In this work, the assessment of designed virtual core-shell nanoparticle (VNP) models led us to the new designs of UCNPs, such as …@Er, Yb@Er, Yb@YbEr, which were experimentally evaluated as donor nanoparticles and compared to the simulations. Moreover, the specific properties of lanthanide-based upconversion motivated us to analyze not only steady-state luminescence and luminescence decay responses of both the UNCP donor and the sensitized acceptor, but also the effects of their luminescence rise kinetics upon RET was discussed in newly proposed disparity measurements. The presented studies help to understand the role of energy-transfer and energy migration between lanthanide ion dopants (due to their concentration and

spatial distribution) and how the architecture of core-shell UCNPs affects their performance as FRET donors to organic acceptor dyes.

KEYWORDS Förster resonance energy transfer, lanthanide doped nanoparticles, photon upconversion, biosensors.

1. INTRODUCTION

Förster Resonance Energy Transfer is a process of short range (roughly 1 – 10 nm [1,2]) dipole-dipole resonance energy transfer (RET) between excited state of a luminescent donor (***D***) and ground state of acceptor (***A***) molecules, which occurs under specific conditions of spectral overlap of ***D*** emission with ***A*** absorption and close proximity of the two molecules. This phenomenon concomitantly results in (i) decreased ***D*** emission intensity, (ii) occurrence of RET-sensitized ***A*** emission (in the case the ***A*** is fluorescent) and (iii) shortening the observed luminescence lifetime of ***D*** in presence of the ***A*** ($\boldsymbol{\tau_{DA}}$) compared to ***D*** alone ($\boldsymbol{\tau_D > \tau_{DA}}$) (Eq. S1). The occurrence of RET-sensitized ***A*** fluorescence and RET-induced ***D*** quenching have been widely used as molecular ruler to evidence bio-specific binding interactions between two molecules such as antibody-antigen [3,4] or complementary nucleic acids sequences, [5–7] as well as to study protein conformation changes. [8–10] In case the two interacting components labelled with ***D*** and ***A*** are bound to each other, the ***D-A*** distance can become sufficiently short to enable RET.

Despite advantageous features and practical applications of RET in biosensing, clinical diagnostics and bioimaging, numerous technical issues hinders its even wider adoption in biotechnology. [11–13] In case of organic fluorophore acceptors, there are several troublesome features, which are difficult or impossible to overcome. For instance broad and partially overlapping excitation or emission

bands of ***D*** and ***A***, which require deconvolution of emission for quantitative studies, photobleaching of ***D*** or ***A*** molecules, radiative reabsorption of ***D*** emission by ***A*** molecules and the inherent features of ***D*** and ***A*** molecules, such as solvato-, halo- or biochromism, as well as short and environment sensitive fluorescence lifetimes in pico- or nanosecond range, which often complicate data acquisition and interpretation.[14] Therefore, new fluorescent ***D*** and ***A*** alternatives are sought, to avoid the major disadvantages of conventional methodology and materials.

One of the alternative ***D*** species are luminescent lanthanide ions, whose emission typically exhibits multiple narrow emission bands, which makes it easier to find spectrally compatible ***A*** and to minimize the ***D*** emission at ***A*** emission wavelength. Moreover, lanthanide luminescence typically exhibits large (anti)Stokes shift, that minimizes the cross-excitation of ***A*** upon excitation of ***D***. [15,16] Lanthanide compounds have often excellent photostability (although some ligand-metal complexes still can suffer from photobleaching) and long micro- to millisecond luminescence lifetimes, which renders them suitable to time-resolved (time-gated) luminescence detection in order to temporally separate the directly excited ***A*** emission (short lifetime) from the sensitized ***A*** emission (prolonged lifetime) and, at the same time, circumvent the sample background autofluorescence generated by short wavelength photoexcitation. [17,18] Thus, the time-gated detection of downshifted lanthanide luminescence enables highly sensitive RET-based biosensing, but also complicates and slows down the luminescence readout and imaging of the RET process. In this paper we will focus on lanthanide-doped upconverting (UC) nanoparticles (UCNPs,) which, in contrast to downshifted lanthanide luminescence, provide autofluorescence free detection also in steady state measurement.

The UCNPs, for example $NaYF_4$: Yb^{3+}, Er^{3+} nanoparticles with a few tens of nanometers in diameter, have an exceptional capability to generate visible or far-red luminescence emission under

near-infrared (NIR) photoexcitation providing them unique advantages as RET donors.[19] The NIR excitation and anti-Stokes emission of UCNPs enables spectral elimination of the background autofluorescence facilitating affordable detection (in terms of cost and complexity), and results in absence of directly excited $\boldsymbol{A}$ emission when they are used as $\boldsymbol{D}$ species in RET with conventional emitting organic dyes. The NIR excitation and the total elimination of the autofluorescence are desirable features for bioassays also because they can simplify sample processing and allow to perform assays in highly colorful, highly absorbing or autofluorescent samples such as whole blood or tissue. [20] Up to now, UCNPs have been exploited as donors in RET with numerous types of acceptors, such as organic dyes (e.g. Rose Bengal, [21,22] Cy3.5, [23] rhodamine B [24] a DBD-6 small organic dye [25] and others [26]), but also with inorganic nanoparticles (quantum dots, [27–36] gold nanoparticles [14] or even lanthanides themselves [37]). Wide range of possible UCNP RET applications have been also demonstrated, [15,38,39] for example in solar-energy H_2 generation, [40] photocatalysis, [29,36,41–45] (bio)detection [22,32,35,36,44–47] or bioimaging. [17,48] Nevertheless, despite multiple advantages, the utilization of UCNPs as RET donors have been found to be more complicated than with conventional single molecule fluorophores originally studied by Förster, and additional studies are required to understand how to optimize the compositional architecture of luminescent UCNPs donors in RET and circumvent their known limitations.

First of all, individual lanthanide-doped UCNPs or down-shifting LnNPs cannot be considered as single donor molecule in a classical sense, [1,49] because such single nanoparticle contains typically hundreds or even thousands of activators such as Er^{3+} ions (as donors $\boldsymbol{D_i}$) and the surface of such donor nanoparticle (DNP) can accommodate many acceptor molecules ($\boldsymbol{A_j}$). Therefore, in relation to a single nanoparticle, numerous $\boldsymbol{D_i}$-$\boldsymbol{A_j}$ pairs can potentially fulfil the conditions required for RET to occur. Even more complex situation is faced in UCNPs, where the activator ions (which are effectively the donors) are typically sensitized by around 10 times larger amount of Yb^{3+} ion sensitizers ($\boldsymbol{S_i}$). Typically for

UCNPs, the long wavelength photoexcitation is matching the sensitizers absorption, which through long living metastable levels transfer their energy to intermediate manifolds of individual activators – donors ($\boldsymbol{D_i}$), to eventually reach their upconversion luminescent excited electronic levels. Ultimately, these donors, under Förster conditions (i.e. spectral overlap and short distance between D and A), are capable to non-radiatively (RET) or radiatively transfer energy further to acceptors ($\boldsymbol{A_j}$). In the first approximation, increased concentration of $\boldsymbol{D_i}$ ions in the UCNPs shall be beneficial for their use as RET donors, but concentration quenching between neighbor ions is a well-known downside of lanthanide emitters.[50–54] The upconversion is typically sensitized by Yb^{3+} ions, which have proven to enhance the absorption cross section of single UCNPs and thus improve their brightness and external upconversion quantum efficiency[55]. But increased content of Yb^{3+} ions was also found to enhance energy migration within the entire NPs volume[56–63] and thus make DNPs also vulnerable to efficient internal quenching on defects[63,64] and surface quenching in aqueous solutions. [20,53,57,65] The actual $\boldsymbol{D_i}$-$\boldsymbol{A_j}$ RET phenomenon is therefore preceded with a complex interplay of multiple excitation, energy cross-relaxation and migration steps between various metastable multiplets and quenching pathways, including both sensitizer and activator ions as well as surface states (Fig. 1).[65]

The role of individual activator ions ($\boldsymbol{D_i}$) within a single UCNP in RET is further defined by their distance from individual acceptor molecules on the NPs surface – the equation for RET efficiency is presented in Eq. S1. This is important, because UCNPs are inherently not capable to bio-specifically recognize biological targets, but require proper bio-functionalization. While the procedures to decorate these NPs with appropriate bio-recognition molecules (such as antibodies and oligonucleotide probes) have been successfully developed, the major obstacle is the fact, that the $\boldsymbol{A_j}$ molecules are thereby translocated further away from the surface of NPs and from the actual donors $\boldsymbol{D_i}$ [35,66,67]. Due to inverse 6^{th} power distance dependence (defined by dipole-dipole interaction scheme of RET mechanism) the

increased $\boldsymbol{D_i}$ to $\boldsymbol{A_j}$ distances can result in strongly reduced RET efficiency (Eq.S1). Nevertheless, the great advantage of UCNPs is the possibility to design core-(multiple) shell nanoparticles and intentionally select most appropriate chemical composition architectures aiming to optimally satisfy the requirements of RET based biosensing [26,68–70] , provide additional functionality [71–76] or pre-defined spectral properties. [60,61,73,77–79] Despite numerous studies have been undertaken, the subject is far from being well understood. Beside conventional (core only or active-core-passive shell) UCNPs applied for RET based bio sensing, [21,47,80–87] more sophisticated core-shell designs have been proposed and studied trying to improve RET efficiency and enhance limit-of-detection in future assay applications[61,88]. These studies evaluated (i) increased surface to volume ratio of donor nanoparticles by reducing the size of $\boldsymbol{D}$ filled core nanoparticle, aiming to increase the relative number of superficial $\boldsymbol{D_i}$ ions per particle. [33,89] More frequently, distance dependent RET from $\boldsymbol{D_i}$ to $\boldsymbol{A_j}$ was studied by (ii) adjusting shell thickness of active core-passive shell nanoparticles, [21,27,47,90,91] and/or (iii) using passive-core-active-shell nanoparticles with shell $\boldsymbol{D_i}$ ions exposed at the surface [23,33,92]. Other distance dependent mechanisms were also proposed and/or experimentally verified, such as (iv) photon avalanche [93] , (v) core-shell designs, which exploits upconverted energy diffusion through Gd^{3+} network to Tb^{3+} or Eu^{3+} RET donor ions [54,57,62] or (vi) dye sensitized UC with tightly packed 800CW dye antenna anchored to the surface, which combined low energy migration zone, antenna enhanced absorption, limiting exposure of Yb^{3+} and Er^{3+} to surface quenchers. These methods were suggesting overall enhanced bio-sensitivity as compared to conventional up-converting nanoparticles.

In this work we have investigated the influence of the compositional architecture of the core@shell UCNPs on the capability to detect $\boldsymbol{D}$-$\boldsymbol{A}$ interaction in the most sensitive manner. The compositional term architecture describes here intentionally designed volumetric distribution of Yb^{3+} sensitizers and Er^{3+} activators - donors in core-shell UCNP donor nanoparticles. Answering the question

how to increase the ***D-A*** RET efficiency and how to reinforce the change in total ***D*** or ***A*** luminescence intensity or shorten ***D*** decay upon RET (reported by decrease in ***D*** emission intensity, increase of sensitized ***A*** emission intensity and shortening of ***D*** decay upon RET), shall be proceeded with a question how to increase a fraction of $\boldsymbol{D_i}$ ions being susceptible to the presence of $\boldsymbol{A_j}$. However, due to complex nature of energy transfer processes leading to upconversion and energy migration, answering the latter question, may not guarantee solving the former issue.

We started with developing a virtual nanoparticle (VNP) model of Er^{3+} and Yb^{3+} co-doped β-$NaYF_4$ core-shell UCNPs and performed simulations and quantitative comparison of the behavior of different architectures of UCNPs under zero up to full possible surface coverage of ***D*** nanoparticles with ***A*** molecules (subchapter 3.1, chapter S1 with Fig.S1-S5 and Table S1-4). In particular, based on $\boldsymbol{D_i}$ distribution in VNP, histograms of $\boldsymbol{D_i}$-$\boldsymbol{A_j}$ distances were calculated to simulate the effect of the $\boldsymbol{A_j}$ on the luminescence kinetics of the ensemble of $\boldsymbol{D_i}$ ions within single nanoparticle. The VNP models permitted to rank various architectures regarding the FRET efficiency, brightness and 'responsiveness' aiming to correlate UCNP compositional architectures with their expected suitability for RET based sensing. Despite the VNP model considered only direct RET from static $\boldsymbol{D_i}$ to $\boldsymbol{A_j}$ and so far excludes the role of sensitizer network, energy-migration and subsequent re-excitation of already relaxed $\boldsymbol{D_i}$, the conclusion drawn from the simulations were further useful to design, synthesize and experimentally evaluate a set of core-shell UCNP architectures with different distribution of sensitizers and activators (subchapter 3.2, chapter S2). Next, in a subchapter 3.2, we experimentally study the spectral and kinetic properties of a series of Er^{3+} and Yb^{3+} co-doped β-$NaYF_4$ core-shell materials upon FRET to Rose Bengal acceptor molecules at various concentrations. In particular, we synthesized undoped core and active shell doped with 2% Er^{3+} (...@Er), core doped with 20% Yb^{3+} and shell doped with 2% Er^{3+} (Yb@Er) and six samples with the same core 20% Yb^{3+} and shells co-doped with 20%Yb^{3+} and 2% Er

(Yb@Yb,Er). To get additional understanding, the latter architecture (presented in SI) was made also with rising (0.1%, 0.2%, 0.5%, 3%, 4%, 5%) concentration of Er^{3+} (named respectively Yb@Yb_0.1Er, Yb@Yb_0.2Er, Yb@Yb_0.5Er, Yb@Yb_3Er, Yb@Yb_4Er, Yb@Yb_5Er). These UCNPs were studied as FRET donors both in spectral and time domain measurements with various concentrations of Rose Bengal acceptor attached directly to the surface of the NPs. Interesting, experimental observation were made, such as the …@Er, Yb@Er and Yb@YbEr samples showed different steady-state and kinetic response to acceptor presence, despite the same 'constellation' configuration (the *"...@Er"* motif) of the donor ions against NP surface (and the acceptor molecules on this surface) exists in all these samples when taking the $\boldsymbol{A_j}$ perspective. Moreover, we found that the sensitizer network can facilitate rapid 're-charging' of $\boldsymbol{D_i}$ once relaxed upon FRET, which ultimately hinders luminescence decay based analysis of FRET efficiency, but on the other hand we noticed that luminescence rise kinetics is affected by the acceptor presence. These studies shine new light on the fundamental role of compositional architecture, inter-relationships between co-dopants and the up-conversion processes that are preceding the energy transfer to acceptor. The suitability of these novel UCNPs as donors for FRET based sensing is profoundly discussed.

2. MATERIALS AND METHODS

2.1. Synthesis Of Nanoparticles

Yttrium oxide (99.99%), ytterbium oxide (99.99%), and erbium oxide (99.99%) were purchased from Alfa Aesar. Dry DMF (99,8%), Nitrosonium tetrafluoroborate (95%), Rose Bengal (95% dye content), Oleic acid (OA, 90%) and 1-octadecene (ODE, 90%) were purchased from Sigma Aldrich.

Acetic acid (99.5–99.9%), ethanol (96%), n-hexane (95%), methanol (99.8%), ammonium fluoride (98%), toluene (99,5%), acetonitrile and sodium hydroxide (98.8%) were purchased from Avantor Performance Materials S.A. (Poland). All chemical reagents were used without further purification. The materials were synthesized according to method described in previous publications [78,94].

2.2. Preparation Of Precursor

In general, the rare earth acetate precursor was prepared by mixing stoichiometric amounts of rare earth oxides (Y_2O_3, Yb_2O_3, Er_2O_3) with 50% aqueous acetic acid and heating the mixture to 200 °C for 120 min under pressure. The final precursor was obtained by evaporation of residual acid and water in rotary evaporator, and further drying at 130 °C for 12 h.

2.3. Preparation Of Core And Core@Shell Material

In a typical synthesis, the prepared dried mixture of $(CH_3COO)_3RE$ precursors (where RE = Y, Yb or Er at preferred ratio, and total amount of 2 mmol) were added to the three-neck flask with OA (12 ml) and ODE (30 ml). The solution was stirred under nitrogen atmosphere and heated slowly to 140 °C, followed by degassing under vacuum for 30 min to remove oxygen and water. After evaporation of residual water, the nitrogen atmosphere was maintained during the synthesis. Then, the reaction temperature was decreased to 50 °C, and during this time, solutions of ammonium fluoride (8 mmol, 0.2964 g) and sodium hydroxide (5 mmol, 0.2 g) dissolved in methanol (15 ml) were added. The reaction mixture was stirred for 30 min at 50 °C. Then, the temperature was increased to 80 °C and the mixture was kept at this temperature for 30 min to evaporate methanol. After that, the reaction temperature was increased quickly to 300 °C and kept at this temperature for 60 min under nitrogen atmosphere. After the UCNPs formation the mixture was allowed to cool to room temperature. The UCNPs were precipitated by addition of ethanol and isolated by centrifugation. For purification, the resulting pellet was dispersed in a minimal amount of n-hexane and again precipitated with excess ethanol. The

final product was isolated by centrifugation. and dispersed in 12 ml n-hexane. For the synthesis of core@shell UCNPs, the following changes in the reaction procedure were introduced. After initial shell precursor mixing and dissolving in OA and ODE at 140 °C, the mixture was cooled to 80 °C and the solution of core UCNPs (2 mmol) was added. The molar ratio of lanthanide content between core and shell was 1:1. The reaction solution was maintained at 80 °C to remove n-hexane. Then, the temperature was lowered to 50 °C and methanolic (15 ml) solutions of ammonium fluoride (8 mmol, 0.2964 g) and sodium hydroxide (5 mmol, 0.2 g) were added. The next steps of the synthesis were analogous to the previously described procedure used for core synthesis. Finally, the UCNPs were precipitated and centrifuged using the same procedure mentioned above. The final product stabilized with OA ligands was dispersed in 5 ml of chloroform ($CHCl_3$).

2.4. Removal of Oleic Acid

To remove the oleic acid ligands from the surface the 8 mg of UCNPs was transferred to Eppendorf tube, then after the centrifugation (30 min, 16900 g) and removal of the supernatant, 500 µl of hexane was added. The mixture was sonicated as long as the pellet had been suspended. After that, 400 µl of acetonitrile and 100 µl of 0.16 M $NOBF_4$ in acetonitrile were added to the tube, and solution was mixed until the particles were transferred from the upper hexane layer to lower acetonitrile layer. In the next step the hexane layer was removed carefully with a pipette. Finally the particles were precipitated by adding 500 µl of toluene, vortexed, centrifuged (30 min, 16900 g) and after removal of the supernatant re-dispersed in 100 µl of Dry DMF.

2.5. Rose Bengal Dye Titration

Two Rose Bengal titration series were performed for each particle batch: one with and the other without phosphate buffer. 0.4 mg of oleic acid stripped UCNPs were added to the Eppendorf tube. Then phosphate buffer (1 ml) was added to the one series of the samples. After 15 minutes of incubation the

dye was added to obtain six different final concentrations of RB (0, 2.9, 9.8, 29.5, 98.3 and 294.8 $\times 10^{-6}$ M). Then DMF was added to obtain the same total volume of the sample which was equal to 500 cm^3.

2.6. Nanoparticles Characterization

Powder diffraction data (Fig. S6) were collected on an X'Pert PRO X-ray diffractometer with a PIXcel ultrafast line detector, a focusing mirror, and Soller slits for Cu Kα radiation. The measurements were done in a Bragg–Brentano geometry in the 10–120 2Θ range. The XRD patterns were assigned using the Joint Committee on Powder Diffraction Standards (JCPDS) database. The emission spectra and decay kinetics of the UC-emission bands at 540 nm were measured with a FLS 980 (Edinburgh Instruments) equipped with a 976 nm photoexcitation wavelength (maximal CW power for this diode is equal 8 W) fractionated (max 25% duty cycle) laser diode (Spectra-Laser, Poland). Alternative home-made optical setup was designed, which exploited a PMT (Thorlabs, PMT2101) and a digital function generation and digital oscilloscope (TiePie HS5), which was used to record rise and decay kinetics. At least 1000 pulses were averaged to improve the signal to-noise ratio. The decay curves were fitted with rise/decay, single or double decay models using the software Origin 8.5.

2.7. Virtual Nanoparticle (VNP) Crystal Model Design and Analysis

Virtual nanoparticle model (Fig. S3) is a computer model of nanocrystal. VNP was designed, based on crystal lattice and position of respective Y^{3+} ions in unit cell (Fig. S3i), with defining core radius and shell thickness of the core-shell nanoparticle (Fig. 3ii), and also defined dopant percentage (as % of total rare earth ions, i.e. the sum of Y^{3+}, Yb^{3+} and Er^{3+} in core or shell, that were evenly distributed). An even network of possible position of acceptor molecule on the surface on VNP was defined (Fig. S3iii). There were different nano-architectures defined (Fig. S3iv), such as small, medium size and large core only UCNPs (20Yb2Er), active-core-undoped-shell (20Yb2Er@...), undoped-core-

active-shell (…@20Yb2Er) for 2% and 5% Er^{3+} co-doping (Fig. S3iv). Next, based on phenomenological Förster distance R_0 (SI, chapter 1.2.) the distances between donor (Er^{3+}) ions and the nearest acceptor (RB dye) molecules (Fig. S3v), histograms of shortest $\boldsymbol{D_i}$-$\boldsymbol{A_j}$ distances for each $\boldsymbol{D_i}$, histograms of $\boldsymbol{D_i}$ lifetimes in the presence of variable $\boldsymbol{A}$ concentration (Fig. S3vi), using the shortest $\boldsymbol{D_i}$-$\boldsymbol{A_j}$ distance for each $\boldsymbol{D_i}$, were calculated using Eq. SI1, which enabled to simulate the $\boldsymbol{A}$ concentration dependent VNP $\boldsymbol{D}$ luminescence lifetimes (Fig. S3vii), to finally get the corresponding expected luminescence decays of donor nanoparticles and $\boldsymbol{A}$ surface coverage dependent RET efficiency (η_τ) calculated by the integrated luminescence kinetics (Fig. S3viii). The details of the upconversion RET and modelling of upconversion RET from VNPs is explained in SI, chapters 1.1. and 1.3., respectively.

3. RESULTS AND DISCUSSION

Three different strategies can be proposed to overcome the disadvantages of conventional lanthanide doped nanoparticles as RET donors. These are either i) reducing the size of the $\boldsymbol{D}$ nanoparticle, ii) exploiting energy migration from $\boldsymbol{D_i}$ NPs center to the surface $\boldsymbol{D_i}$ [95] or iii) bringing the individual $\boldsymbol{D_i}$ as close to the surface of the nanoparticle as possible. [88,96] Similar approaches have been experimentally studied e.g. by Muhr et all [97], Valanne et al. [10] , Meyer et al.[98], R .Deng et al. [62,95] , Zhang X. et al.[88] and C. Siefe et al[70]. Actually, the strategies, are diverse versions of the same approach, where the key idea is to increase the relative number of close-to-surface effective $\boldsymbol{D_i}$ in respect to number of internal ('volumetric') donor ions. These various strategies, schematically presented in Fig. 1, were first evaluated by us using the VNP models (Fig. S3) and then experimentally studied using synthesized core-shell nanoparticles.

3.1. Theoretical considerations on RET with lanthanide doped nanoparticles

Although large core-only UCNPs (Fig. 1a) should, in principle, be significantly brighter than most of other designs, such as e.g. undoped-core-active-shell (Fig. 1b; …@20Yb2Er), small core-only nanoparticle (Fig. 1d; small 20Yb2Er) or sensitized-core-active-shell (Fig. 1e; 20Yb@20Yb2Er), their major drawback as RET donors is that the activator ions within the center of donor NP are contributing to the total luminescence, but they are beyond the Förster distance, thus are not directly susceptible to the presence of acceptors on the NP surface. Ultimately, such UCNPs have a large number of $\boldsymbol{D_i}$, but only small fraction of $\boldsymbol{D_i}$ (out of all available) are capable to RET to $\boldsymbol{A_j}$, and thus the ratio of RET sensitized $\boldsymbol{A_j}$ emission to $\boldsymbol{D_i}$ emission is low. The large fraction of $\boldsymbol{D_i}$ not directly capable to RET to $\boldsymbol{A_j}$ can also facilitate the contribution of radiatively excited $\boldsymbol{A_j}$ emission. For small (Fig. 1d), undoped core and active-shell (Fig. 1b), and sensitizer doped core and active-shell (Fig. 1e) UCNPs, most of the $\boldsymbol{D_i}$ ions per single DNP are capable to RET to the $\boldsymbol{A_j}$ anchored on the particle surface and thus the relative ratio of $\boldsymbol{D_i}$ directly susceptible to $\boldsymbol{A_j}$ is increased. The latter two designs, i.e. undoped core and active-shell (Fig. 1b), and sensitizer doped core and active-shell (Fig. 1e), should exhibit similar direct susceptibility of $\boldsymbol{D_i}$ to the presence of to $\boldsymbol{A_j}$.

The sensitizer doped core and active-shell (20Yb@20Yb2Er) UCNPs, owing to larger number of Yb^{3+} ions per particle, should exhibit higher absorption cross section and thus potentially brighter upconversion luminescence emission. However, due to energy migration through the sensitizer ($\boldsymbol{S_k}$) network, the entire particle volume can be strongly affected by internal[63] or surface quenching (associated to O-H vibrational overtones and vibrations of other organic ligands), decreasing the external quantum yield and result in reduced sensitization of $\boldsymbol{D_i}$ [20]. The efficient energy migration, however, can also channel the cumulative excited-state energy from the $\boldsymbol{D_i}$ and $\boldsymbol{S_k}$ (originally beyond the Förster

radius) to the superficial $\boldsymbol{D_i}$ involved in RET. This is facilitated by the long-living excited-states of the volumetric $\boldsymbol{D_i}$ and $\boldsymbol{S_k}$ ions, and the latter may therefore act as energy reservoir to 're-charge' the superficial $\boldsymbol{D_i}$ that have already been deactivated upon RET to short living $\boldsymbol{A_j}$. This would render such DNP nanoparticles to work well in steady-state luminescence intensity domain enabling also the volumetric $\boldsymbol{D_i}$ to indirectly participate in RET. However, due to the time lag owing to the energy migration and the repopulation, the luminescence decay behaviour of such donor nanoparticles would be less susceptible to the presence of $\boldsymbol{A_j}$. As a consequence of the 're-charging', the determination of RET efficiency from the change of luminescence lifetime of DNP nanoparticles would no more be possible.

The surface quenching facilitated by energy migration is common to most of the architectures lacking passive external shell (Fig. 1a, b, d, e) which has been proven to prevent the parasitic surface quenching, improve upconversion luminescence intensity and external quantum yield [99]. However, while such passivated nanoparticles optimized for high brightness are good luminescent labels, they compromise RET based sensing, because superficial $\boldsymbol{D_i}$ ions are displaced from the $\boldsymbol{A_j}$ molecules anchored on the NP surface. In practical applications, the capability to RET to $\boldsymbol{A_j}$ is even weaker as the recognition molecules displace the $\boldsymbol{A_j}$ acceptor molecules further away from the surface and therefore increase the $\boldsymbol{D_i}$ to $\boldsymbol{A_j}$ distances and further reduce RET efficiency[93]. The thickness of the superficial protective shell must thus be carefully optimized or alternative $\boldsymbol{D_i}$ ions or excitation schemes without Yb^{3+} sensitizers must be employed. [93,95] The compositional and architectural optimization of UCNP donor nanoparticles for up-conversion RET is thus far from trivial and different architectural designs of $\boldsymbol{D}$ nanoparticles may be preferred either for luminescence intensity or for the luminescence decay based detection.

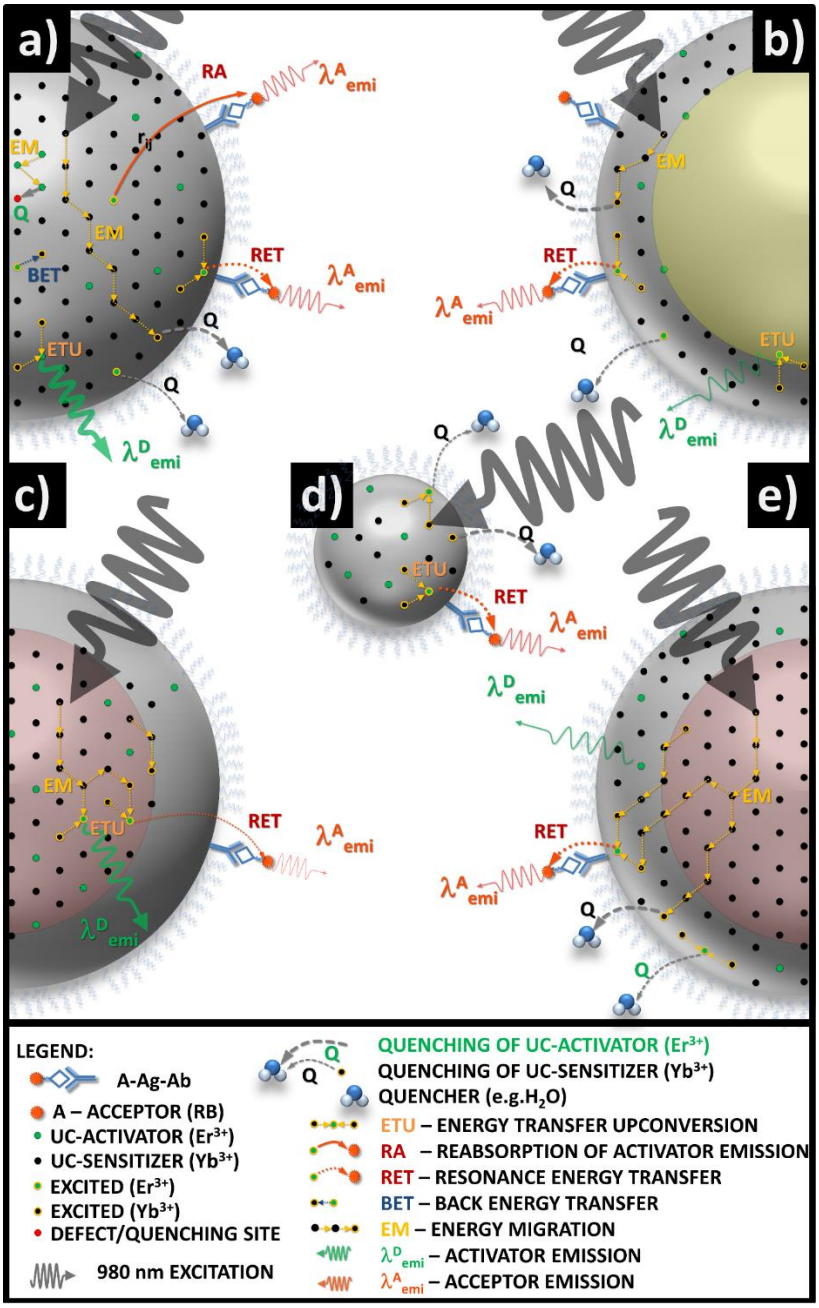

Fig. 1 Schematic illustration of various composition architecture design strategies for more efficient UCNP donors dedicated for homogenous RET bioassays. a) large core only UCNPs (20Yb2Er) b) undoped-core-active-shell (...@20Yb2Er), c) active-core-undoped-shell (20Yb2Er@...), d) small core-only nanoparticle (small 20Yb2Er), e) sensitized-core-active-shell (20Yb@20Yb2Er). Depending on the UCNP design, one may expect various contribution of phenomena such as surface quenching of

sensitizers (Yb^{3+}) or surface/defects quenching of activators (Er^{3+}) (Q), energy transfer up-conversion (ETU), resonance energy transfer (RET), back-energy transfer (BET) and Yb-Yb and Er-Er energy migration (EM) efficiency, as well as the luminescence emission of the activator and acceptor, and radiative energy transfer, such as reabsorption of the activator emission (RA). The existence and the probabilities of the above mentioned processes (such as Q, ETU, RET, BET, EM, D and A emission and RA), are schematically illustrated by the presence of corresponding symbols (see legend) and the line thickness, respectively. For sake of simplicity these processes have been schematically shown in some of architectures, but actually may occur in all NP types depending on concentration of sensitizer and activator ions.

There are generally three modelling strategies, e.g. virtual nanoparticle model (VNP), differential rate-equation modelling (DRE) and Monte-Carlo (MC) modelling, which are suitable to analyze various aspects of lanthanide doped nanoparticles behavior as RET energy donors. In our work we wanted to understand to role of donor ions distribution on RET efficiency, but we have additionally learned how important energy migration is for kinetics based UC RET assays under quasi continuous wave pumping. Therefore, beside VNP and DRE models, the MC modelling is necessary for further comprehensive understanding of dynamic processes occurring in the UC RET system. Nevertheless, our VNP model helps to explain fundamental differences between UC RET and conventional molecular FRET between single D and A molecules. Secondly, the VNP model helped to indirectly understand the role of energy migration. The quantitative differences between the model decay behavior and experiments strongly supports the hypothesis that the energy migration, energy storage and 'recharging' cannot be neglected when practical applications are considered. The effect of dopant concentration (and energy migration) on UC RET efficiency was further evidenced by the final experiment where only the Er concentration was titrated.

It is important to highlight we studied RET using up-conversion, which is a very specific form of luminescence. Long 4 ms 980 nm pulses were used to excite Yb^{3+} sensitizer ions, which then through energy up-conversion excite Er^{3+} ions, which ultimately become donors for the Rose Bengal acceptors in the visible spectral range. On the one hand side, the Yb^{3+} ions are required to enable efficient anti-Stokes emission and background free detection, which are critical for bio-sensing. On the other hand, Yb^{3+} ions are also capable to (1) accumulate the pump energy, (2) migrate this energy efficiently over longer distances and (3) repopulate donor ions which affects the kinetics of emission. Moreover, these are Yb^{3+} ions that are (despite their large ca. 9300 cm^{-1} energy gap) highly susceptible to -OH groups quenching. Moreover, to excite Yb^{3+} ions we have used medium CW power (P_{CW} = 10 W) laser diodes controlled by TTL pulses. Although these light sources are widely available, robust, cheap and perfectly suitable to make miniaturized point-of-care reading RET devices, in order to make the UC bright enough pulses of at least 1 ms are needed (the UC builds slowly within few tens up to hundreds of microseconds), which is known to pump many intermediate, long living energy states.

Based on the formalism developed by Förster for molecular RET, the qualitative relationship between the individual r_{DiAj} and effective spectroscopic measures, such as luminescence kinetics or spectra, are intuitively understood also for lanthanide doped DNP. We however wanted to understand this behaviour in a more quantitative way. This is why a virtual nanoparticle (VNP) model was developed (chapter 1.4 in SI). Briefly, the VNPs were designed using crystallographic structure of β-$NaYF_4$. These VNPs were 'co-doped' with sensitizer (Yb^{3+}) and activator (Er^{3+}) ions by substituting Y^{3+} ions at given concentrations. By assuming core radius (R_C) and shell thickness (L_S) of the VNP (Fig. S3i-ii), and various surface coverages with Rose Bengal (RB) acceptor (Fig. S3iii), we were able to establish the numbers and positions of the Er^{3+} donors as well as RB acceptors in the different structures (Fig. S3iv) and thus generate histograms of $\boldsymbol{D_i}$ - $\boldsymbol{A_j}$ distances (Fig. S3v). The VNP model and the developed

mathematical tools (explained below and in SI) were further used to calculate how the RET affects luminescence lifetime of individual $\boldsymbol{D_i}$. As the outcome, the behaviour of different structures was simulated and analysed in terms of $\boldsymbol{D_i}$ luminescence kinetics and overall RET efficiency at various acceptor surface coverages (Fig. S3vi-vii). Thus, the six different architectures of DNPs, small, medium and large UCNPs (VNP:20Yb2Er), active-core-undoped-shell (VNP:20Yb2Er@...), sensitized-core-active-shell for 2% Er^{3+} (VNP:20Yb@20Yb2Er) and 5% Er^{3+} co-doping in the shell (VNP:20Yb@20Yb5Er), were quantitatively compared to answer the question of preferable architecture of UCNPs as DNPs. The simulations assumed that RET effect of $\boldsymbol{A_j}$ on each of the excited $\boldsymbol{D_i}$ can be treated independently, and no synergetic processes, which could rebalance the excited-state energy distribution among the activators, such as energy migration between Er^{3+} ions, are present.

Based on the methodology explained in chapter 1.4 of supporting information (Fig. S1-S5, Table S1-S4), we analyzed the expected luminescence kinetics behavior for various virtual nanoparticle UCNP compositional architectures. Firstly, based on $\boldsymbol{H_r}$ statistics (Fig. 2a) for rising acceptor concentration, we note that more and more $\boldsymbol{D_i}$ ions find $\boldsymbol{A_j}$ sufficiently close to enable RET, and fall into effective RET distance represented by Förster curve. Next, histograms of luminescent lifetimes of individual $\boldsymbol{D_i}$ ions were obtained (Fig. 2b), by calculating $\boldsymbol{\tau_{DiAj} = f(r_{DiAj})}$, with R_0 = 2.00 nm and τ_D= 120 µs. Next, total luminescence kinetics (Fig. 2c) from all $\boldsymbol{D_i}$ ions within single VNP was calculated with Eq. S10. This enabled to ultimately derive $\boldsymbol{A}$ concentration dependent overall energy transfer efficiencies for DNPs from integrated luminescence decay based dose-response curves (Fig. 2d, Eq. S11 quantified versus $\boldsymbol{A}$ concentration). The simulations predicted the effect of RET on the composite $\boldsymbol{D_i}$ luminescence kinetics after pulsed excitation, thus once excited, individual $\boldsymbol{D_i}$ are deactivated by either emitting photons or RETing energy to nearest neighbour $\boldsymbol{A_j}$ molecule. The calculations for every $\boldsymbol{D_i}$

ions present in DNP were based solely on its distance to closest $\boldsymbol{A_j}$ acceptor at the surface and possible interactions and other, more distant $\boldsymbol{A_j}$ were ignored for sake of simplicity. This approach is justified by the fact that the lifetimes of $\boldsymbol{A_j}$ are a few orders of magnitude shorter than the lifetimes $\boldsymbol{D_i}$, thus single acceptor molecule may interact with many different donor ions within the average lifetime of the excited donor. Such analysis enabled to study the role of $\boldsymbol{D_i}$ distribution and composition architecture on the performance of VNPs (SI chapter 1.5, and Fig. S4). The interpretation of the data in Fig 2. is not straightforward, because the RET efficiency of individual $\boldsymbol{D_i}$ ion is related to $\boldsymbol{D}$-$\boldsymbol{A}$ distance with 6th power dependence (see chapter 1.5 in SI) and the distance distribution varies significantly between the compositions and depends on the acceptor surface coverage.

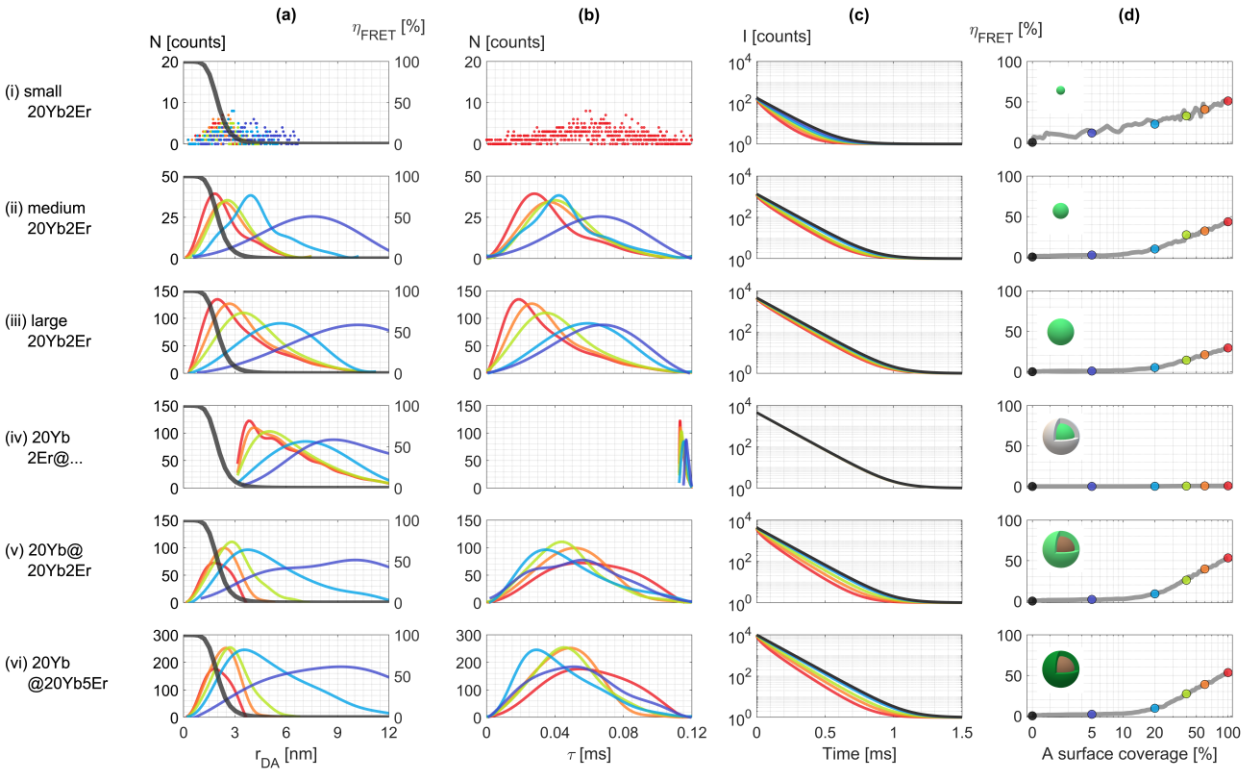

Fig. 2 Results of RET simulation with VNPs as donors and different surface coverages of acceptor molecules. *Various VNPs were simulated (i) small core-only nanoparticle (small 20Yb2Er),*

(ii) medium core-only nanoparticle (medium 20Yb2Er), (iii) large core-only UCNPs (large 20Yb2Er), (iv) active-core-undoped-shell (20Yb2Er@...), (v) sensitized-core-active-shell (20Yb@20Yb2Er) and (vi) sensitized-core-active-shell with increased activator concentration (20Yb@20Yb5Er) versus the concentration of acceptor of the surface of VNPs. The subsequent columns show (a) acceptor concentration dependent histograms $H_r(r_{DA})$ of donor-acceptor distance r_{DA}, (b) the $H_r(r_{DA})$ histograms converted to acceptor concentration dependent luminescence lifetime domain $H_\tau(r_{DA})$ histograms, (c) simulated acceptor concentration dependent donor NP luminescence decays, and (d) acceptor surface coverage dependent energy-transfer efficiencies, i.e. acceptor dose responses on the integrated luminescence kinetics (and the schematic VNPs structure), respectively for all six different VNP structures. Dark grey solid line in (a) indicate RET efficiency curve (right axis) with estimated Förster distance, $R_0 = 2.00 \pm 0.24\ [nm]$. *The colours on (a)-(d) are corresponding to each other, which indicate acceptor concentration – 100%-red ●, 60%-orange ●, 40%-green ●, 20% blue ●, 10% - violet ●, 0% - black ●, i.e. black color on (c) and (d) indicate properties of D-only (without presence of A).*

Theoretically, reducing the size of the core-only UCNPs increases the surface to volume ratio and exposes larger fraction of $\boldsymbol{D_i}$ ions to $\boldsymbol{A_j}$ at the surface and results in enhanced RET efficiency as can be also concluded from the simulation of RET with VNPs. In practice, however, such approach also strongly decreases the upconversion luminescence intensity due to increased surface quenching and reduces the overall upconversion QY.[53,100] This does not necessarily decrease the RET efficiency, as it mostly affects the excitation of the $\boldsymbol{D_i}$ ions and not necessarily the internal QY of excited $\boldsymbol{D_i}$, but nevertheless strongly decreases the intensity of the RET sensitized acceptor emission. The passive shell, on the other hand, would recover the luminescence intensity, but at the cost of increased donor-acceptor

distances and again strongly reduced RET efficiency[21]. It has been shown that for example $NaErF_4$ core NPs, a $NaLuF_4$ shell of 10 nm thickness is required to efficiently eliminate the quenching occurring through phonons of surface ligands and solvent interactions.[101] Because the passive shell was found in the simulation of RET as the worst architecture and due to obvious challenges related to utilization of the small core-only DNP, we focused the experimental work to the core-shell architectures with $\boldsymbol{D_i}$ located in the shell only.

It is obvious from Fig. 2i-iii, column c, that increasing the size of core-only nanoparticles makes such DNPs brighter (based on rising counts), but simultaneously makes them less susceptible to the presence of the acceptor, because the donor luminescence decays become indistinguishable from donor only decay curves. For the passive shell sample (Fig. 2iv), the shell is responsible for shifting vast majority of $\boldsymbol{D_i}$-$\boldsymbol{A_j}$ distances beyond the Förster distance ($r_{DiAj} > R_o$). Thus, the donor luminescence decays are only weakly affected by the presence of acceptors and overall RET efficiency remains low for such DNPs even fully covered with acceptor molecules. One may also note, considering the sensitized-core-active-shell nanoparticles, that the 5%Er^{3+} sample (Fig. 2vi) behaves only slightly different from the 2%Er^{3+} sample (Fig. 2v); nevertheless the histograms on column *a* are slightly narrower and localized closer to short r_{DA} for 5% as compared to 2%. The shorter distances translate to slightly shorter lifetimes in the donor lifetime histograms, but the difference in the lifetime distribution is small. In the 5% Er^{3+} sample almost half of the thousands of donor ions incorporated in single DNPs still have practically the same $\boldsymbol{D_i}$ - $\boldsymbol{A_j}$ distances as in the 2% Er^{3+} sample and the contribution of those donor ions is unchanged. Furthermore, despite more superficial donor ions can be found for higher doping Er^{3+}, also the number of donor ions staying in medium-far distance from acceptors is increased. The increased number of the superficial donors is evidenced only in very early part of luminescence decay

and overall, their contribution to total luminescence decay curve remains marginal, because the luminescence of these donor ions is hidden behind (Fig.S4 column b) the luminescence of donor ions at longer r_{DA} distances – these effects translate to non-significant RET. Thus, the overall simulated RET efficiencies (Fig. 2, column d) calculated by integrating the luminescence kinetics at various acceptor surface coverages do not significantly differ between the 5% and 2% samples, yet the response at low acceptor surface coverage is slightly increased with the high Er^{3+} doping. The largest response in RET efficiency at low acceptor surface coverage, however, is achieved with the small core-only nanoparticles.

Although it is useful to analyze the different core-shell architectures and select best candidates for efficient DNP, the applied VNP model and subsequent simulation of RET is not able to consider at the moment a few important physical phenomena involved. It does not yet take into account $\boldsymbol{D_i}$ quenching by surface ligands and vibrations of solvent, which are competitive processes to RET and especially cause problems in water, organic or multicomponent media.[20] Moreover, the energy migration (EM) between sensitizing Yb^{3+} ions, the cross-relaxation (CR) which occur between Er^{3+} ions or the back energy transfer (BET) from Er^{3+} to Yb^{3+} are not considered in the simulation. With these additional processes (EM, CR and BET) the spectral and kinetic characteristics of the RET system would become even more complicated. Moreover, due to the fact the energy transfer upconversion exploits multiple and long living excited energy states of sensitizer and activator ions, energy transfer processes are pump power and excitation history dependent and the lifetimes of organic acceptor molecules is typically much shorter than the lifetimes of lanthanide excited state, all these further complicates the dynamics of the FRET system.[65,102,103] As we hypothesized, the energy transfer processes within DNPs can result in that $\boldsymbol{D_i}$ ions once relaxed by emitting a photon or upon RET are rapidly re-charged by energy stored

in long-living excited states of sensitizer-activator (Yb^{3+}-Er^{3+}) network. Further, under quasi continuous wave excitation, the luminescence decay of $\boldsymbol{D_i}$ shortened by RET to $\boldsymbol{A_j}$ results in that the excitation cycling of individual $\boldsymbol{D_i}$ participating to RET can be faster than of those $\boldsymbol{D_i}$ not participating to RET. Thus, the emission spectrum of such RET system obtained by steady-state excitation might be different than obtained by pulsed photoexcitation –while the latter was the basis for the here performed simulations. In case the RET provides an efficient relaxation pathway for the excited $\boldsymbol{D_i}$, the steady-state measurement (while the excitation is continuously on) should provide an increased spectral contribution of the RET sensitized $\boldsymbol{A_j}$ emission compared to the pulsed excitation due to the more rapid deactivation and recharging cycle of the $\boldsymbol{D_i}$ upon RET to $\boldsymbol{A_j}$. For practical applications, the increased RET sensitized acceptor emission obtained by the continuous excitation and simultaneous measurement can be beneficial, as in the upconversion luminescence there is no need for time-resolved detection to separate the background autofluorescence or directly excited acceptor fluorescence. In some cases however, such as with highly concentrated or scattering samples, the analysis of the luminescence kinetics could provide a more reliable way to confirm the specific responses. Nevertheless, the simulation of RET with VNPs results gave hints about most favorable architectures, preferably exposing donor ions as much as possible to surface and removing them from the DNP interior.

The simulation results directly demonstrate the beneficial role of increased proportion of superficial $\boldsymbol{D_i}$ ions related to the whole population of all available $\boldsymbol{D_i}$ ions in DNPs. This was evidenced both in small core-only (20Yb2Er) and sensitized-core-active-shell (20Yb@20Yb2Er) samples by a significant portion of $H_r(r_{DA})$ overlap with Förster efficiency curve (Fig. 2i and v,vi, column a). Importantly, the small DNPs exhibit emission intensities which are c.a. 2 orders of magnitude weaker than the other samples, which obviously demonstrate that a proper balance between upconversion luminescence intensity and overall RET efficiency must be considered to develop an optimized solutions. Further, to

achieve high sensitivity at low acceptor surface coverage, it is likely equally beneficial that a single acceptor molecule on the surface of DNP can work as RET acceptor to multiple $\boldsymbol{D_i}$ ions located within the Förster distance range. With the active-core-undoped-shell (20Yb2Er@...) sample (Fig. 2iv), it is clear that the surface passivation (or other surface functionalization layer) inevitably increases all the $\boldsymbol{D_i}$-$\boldsymbol{A_j}$ distances, and the effect of RET at distances $r_{DiAj} > R_0$ is too inefficient to result in noticeable change in the donor luminescence decays. The nonlinear $H_\tau(r_{DA})$ dependence suggests that in all the compositional architectures the contribution of $\boldsymbol{D_i}$ ions at distances beyond the Förster distance is negligible to RET, but the real situation is, however, even more complicated.

3.2. Experimental verification of various DNP core-shell strategies

To experimentally assess the results obtained and the favorable compositional architectures suggested by the simulation of RET with VNPs, a series of Er^{3+} and Yb^{3+} co-doped β-$NaYF_4$ core-shell NPs were synthesized with well-defined crystal structures and morphology (Fig. 3a-d). In addition, our objective was to investigate how the (co-)localization of Yb^{3+}sensitizers and Er^{3+} activators (donors) in core-shell UCNP donor NPs modify the RET efficiency.

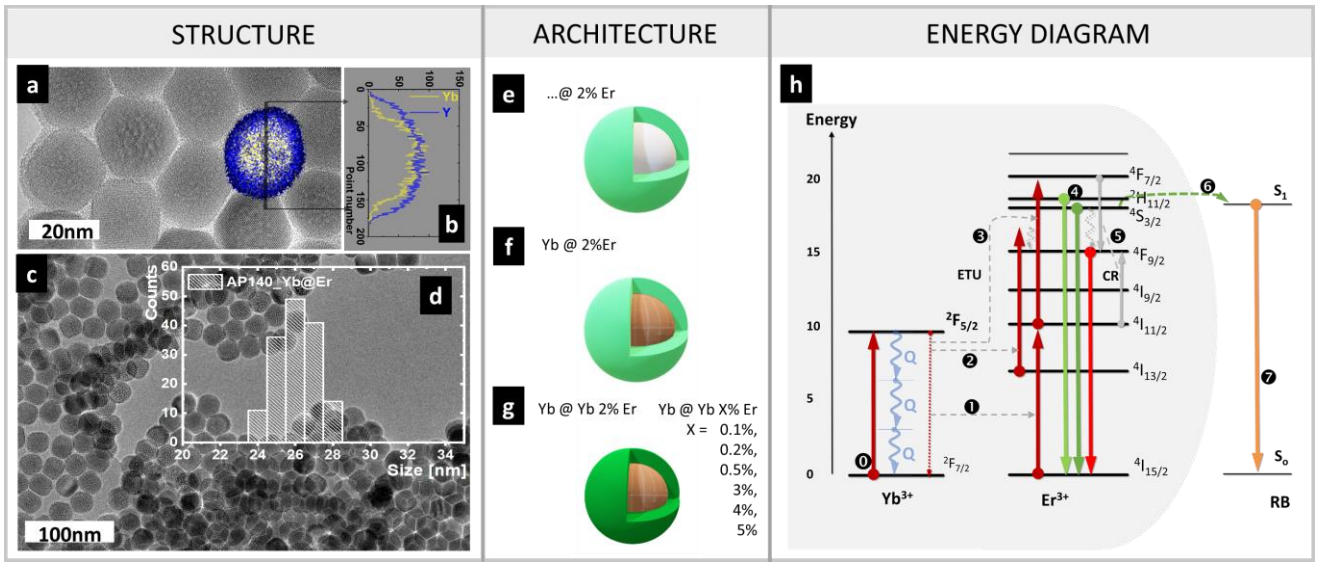

Fig. 3 The material properties (structure), synthesized core-shell nanoparticles (architecture) and Yb-Er up-conversion based RET (energy diagram). Representative (a) TEM, (b) TEM-EDS, (c) large field-of-view TEM and (d) size distribution of Yb@Er Sample. The schematic description of the synthesized nanoparticles: (e) undoped-core-active-shell (...@2Er), (f) sensitized-core-active-shell (20Yb@2Er) and (g) sensitized-core-active-shell (20Yb@20Yb2Er, and additional 0.1, 0.2, 0.5, 3, 4, 5%); (h) energy diagram of energy transfer Yb-Er^{3+} up-conversion based Er-to-RB RET.

A few compositional architectures of the core-shell UCNPs were prepared, namely : (i) empty core and shell doped with 2% Er^{3+} (Fig. 3e), (ii) 20%Yb^{3+} sensitized core and 2%Er^{3+} doped shell (Fig. 3f) and (iii) seven samples with the same 20%Yb^{3+} doped core and shells containing 20%Yb^{3+} and different concentration (0.1%, 0.2%, 0.5%, 2%, 3%, 4%, 5%) of Er^{3+} (Fig. 3g). The three different DNP architectures, with the same Er^{3+} dopant (2%) concentration in the shell, and the identical surface coverage of attached RB acceptor, should provide, in practice, identical $\boldsymbol{D_i}$ - $\boldsymbol{A_j}$ distances and thus indirectly enable studying and understanding the consequences of energy-migration. Further the DNPs

with different Er^{3+} dopant concentrations allow to evaluate the effects of locating multiple $\boldsymbol{D_i}$ donor ions within the Förster distance range of an individual $\boldsymbol{A_j}$. The energy diagram of the Yb^{3+} sensitizer, Er^{3+} activator/donor and RB acceptor schematically explain the RET mechanism (Fig. 3h). Different concentrations of RB acceptors (equivalent to acceptor surface coverages) were directly coordinated onto the oleic-acid stripped UCNPs (SI, chapter 3.1, and Fig. S7) and the emission spectra of the RET systems under steady-state excitation, as well as, luminescence decays (SI, chapter 3.2) at donor (Er^{3+}) and acceptor (RB) specific emission wavelengths, 550 and 590 nm, respectively, were recorded with 2 ms wide excitation pulse. Further, to evaluate the contribution of the radiative energy-transfer, a control experiment with blocking the UCNP surface with phosphate before mixing with RB acceptor was carried out. Thus, in the control experiment (Fig. S7, S10) the equal concentration of RB was present, but not attached on to the surface of the UCNPs. The single layer of RB acceptor attached to the surface compared to the same amount present in the surrounding solution cannot generate significant difference in the overall absorption of donor emission, and thus does not result in significant difference in the quenching of the UCNP luminescence or increase in sensitized RB acceptor emission.

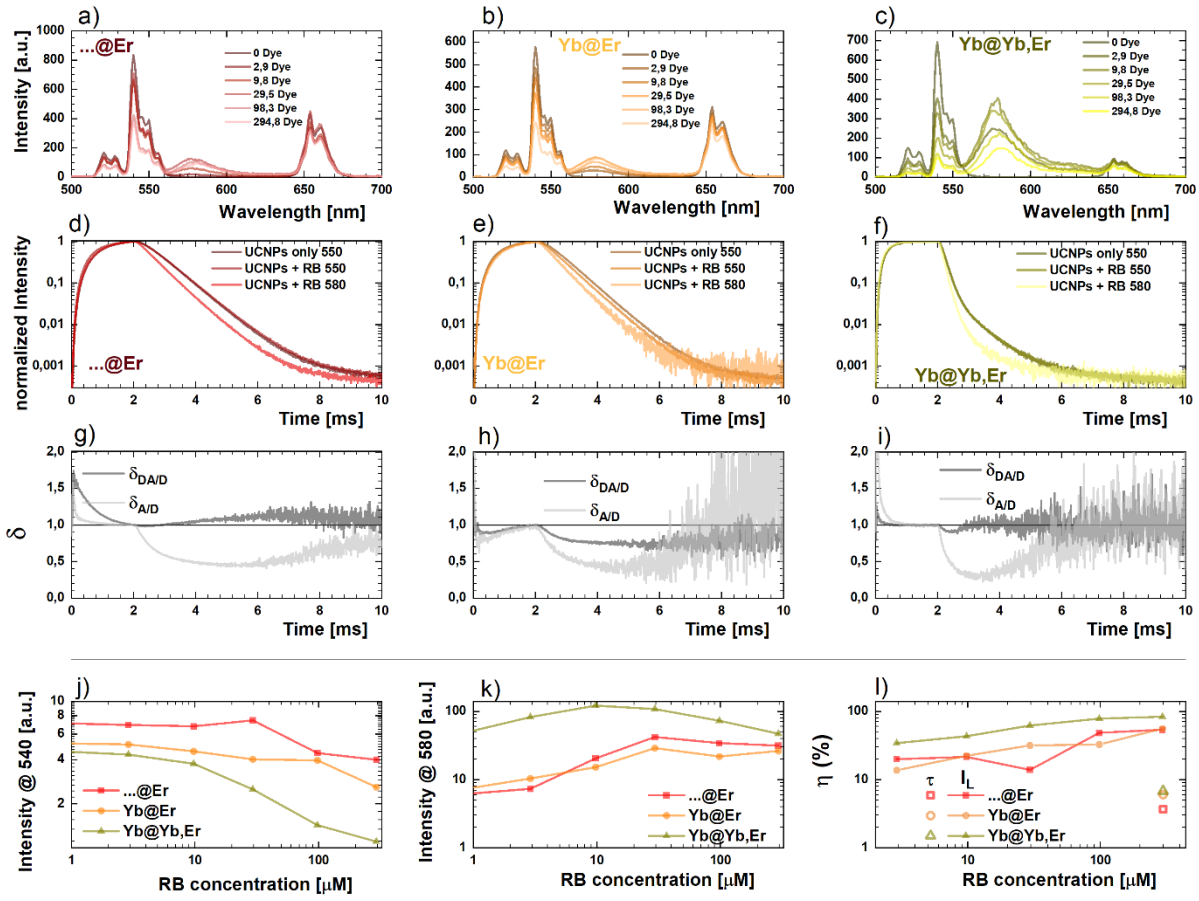

Fig. 4 ***Steady-state luminescence and luminescence kinetic behavior of different DNP architectures in RET experiments with RB acceptor.*** *The steady-state spectra (top-row) and luminescence kinetics (middle row) of (a,d) ...@Er, (b,e) Yb@Er and (c,f) Yb@YbEr DNP architectures were compared. The emission spectra and decay curves (excitation pulse width 2 ms) were recorded from D only and D-A samples under 976 nm photoexcitation for each DNP architecture. The emission spectra (a-c) were measured with a variable and the decays with a fixed (29.5 μM) concentration of RB acceptor attached directly to the surface of DNPs. The luminescence kinetic profiles (d-f) are presented at 550 nm for D only and both at 550 nm and 590 nm for D-A samples. Donor disparity ($\delta_{DA/D} = I_{DA}(t)@550 \,/\, I_D(t)@550$) as well as acceptor disparity ($\delta_{A/D} = I_A(t)@590 \,/\, I_D(t)@550$) are presented in (g-i). The $\delta_{DA/D}$ or $\delta_{A/D}$ = 1 would mean that the D or sensitized A luminescence kinetics in the presence of*

A does not differ from the D only luminescence kinetics. The bottom row panels present the RB concentration and DNP architecture dependency of (j) Er^{3+} luminescence emission intensity at 550 nm, (k) RB emission intensity measured at 580 nm, and (l) RET efficiency based on emission spectra (solid symbols, $\eta_I = \left(1 - \frac{I_{DA}}{I_D}\right) \cdot 100\%$), and efficiency based luminescence lifetimes (open symbols, $\eta_\tau = \left(1 - \frac{\tau_{DA}}{\tau_D}\right) \cdot 100\%$,only for the highest RB concentration).

According to the theory of Förster resonance energy transfer, the non-radiative resonance energy transfer from donor to acceptor should be evidenced by (i) decreased donor emission intensity, (ii) increased sensitized acceptor emission intensity (in case the acceptor is fluorescent), and (iii) the shortened of donor emission lifetime. In case of rapidly decaying acceptor, i.e. when the natural luminescence decay of the acceptor is much shorter than the decay the lanthanide donor, the observed luminescence lifetime of the sensitized acceptor should match the shortened lifetime of the donor. If radiative reabsorption based energy-transfer occurs, which may happen in highly concentrated samples, the first two phenomena would be present, but the lifetime of donor (and the observed lifetime of the sensitized acceptor emission) should stay unaffected. Based on the experimental results it becomes clear that both (i) decreased Er^{3+} donor emission intensity and (ii) increased sensitized RB acceptor emission intensity are present. However, the last feature (iii) – i.e. the shortening of the donor emission lifetime is negligible (Table S5), and does not match the RET efficiency expected from the decrease in the donor emission intensity. The observed lifetime of the sensitized RB acceptor emission, however, is significantly shorter supporting the hypothesis of the non-radiative mechanism. Compared to the emission intensity decrease of the donor, the observed lifetimes of the sensitized acceptor emission seems to underestimate

the observed efficiency of the non-radiative ET transfer processes involved. Further, based on the control experiment, the role of the reabsorption based ET energy-transfer can be concluded minimal. Therefore, the energy-transfer mechanism must be mostly related to RET, but the expected change in the decay of the donor or sensitized acceptor emission is missing or at least too small to explain the observed changes in the donor or sensitized acceptor emission intensity.

Concerning the RET from the perspective of the RB acceptor molecules the three …@Er, Yb@Er and Yb@YbEr architectures are identical - the …@Er motif, i.e. distribution and distances of donor ions in the shell as seen by acceptors is in principle the same for all the three samples. However, considering steady state spectra (Fig. 4 a-c), the Yb@YbEr sample is clearly more sensitive to the presence of already small concentrations of the RB acceptor than the …@Er or Yb@Er samples and it should provide enhanced sensitivity in RET assays compared to other architectures. This is evidenced by RB concentration dependent decrease of Er^{3+} emission at 540-550 nm ($^4S_{3/2} \rightarrow {}^4I_{15/2}$) and the opposite RB emission rise at 570-600nm ($S_1 \rightarrow S_0$). These intensity changes (Fig. 4a-c) are significantly more intense in Yb@YbEr sample (Fig. 4c) when compared to …@Er or Yb@Er samples (Fig. 4a and b, respectively) leading also to improved ratio between the sensitized RB acceptor and the Er^{3+} donor emission intensity in the Yb@YbEr sample (Fig. 4j). The probable reason for this is an efficient energy migration and continuous recharging of the Er^{3+} donor ions relaxed non-radiatively upon RET during the steady-state excitation. The Er^{3+} donor ions deactivated rapidly upon RET, would thus be recharged faster than those donors which are not participating to RET. In consequence, their relative contribution to the emission of sensitized acceptor would be enhanced. The VNP model based RET analysis, however, assumed pulsed excitation and excluded the possible effect of continuous excitation or delayed recharging of the deactivated donor ions. The Er-Yb back energy transfer could also be possible due to the resonance of the $^2F_{5/2}$ of Yb^{3+} and $^4I_{11/2}$ of Er^{3+} (similar ~10100 cm^{-1} energy gap to respective ground

state) and can facilitate energy transfer from more distant Er^{3+} donor ions to those closer to the RB acceptors. In consequence, larger volume of the DNPs could be susceptible to RET than enabled by just the Förster distance as was assumed in the VNP model based analysis of RET. It is clear, there is a large excess of donor ions compared to RB acceptors - based on the VNP model for Yb@Yb,xEr, where x was 2% or 5%, 4329 or 10821 Er^{3+} ions were calculated respectively per single 28 nm in diameter DNP (Table S2), whereas the surface can accommodate up to 441 RB acceptor molecules. The role of energy-migration and recharging is further facilitated by the large discrepancy of the excited state life-times of Er^{3+} donor and Yb^{3+} sensitizer (tens-to-hundreds of microseconds) compared to the lifetime of the RB acceptor molecule (approximately <10 ns), and a single RB acceptor molecule is thus capable to successively and repeatedly deactivate multiple Er^{3+} donor or Yb^{3+} sensitizer ions through a single Er^{3+} donor Er^{3+} donor luminescence lifetime. It should be noted that even in the steady-state excitation regime, the recharging of the deactivated Er^{3+} ions would not increase their relative contribution to the sensitized RB acceptor intensity (as now is clearly visible in Yb@YbEr), unless they are deactivated non-radiatively i.e. by resonance ET process. Overall, this would result in local accelerated deactivation upon presence of the RB acceptor in contrast to possible radiative ET processes. However, in the case of Er^{3+} donors being relaxed by RET, the question arises - why changes in donor luminescence decays upon RET interaction are barely visible or absent? Even though the decay of the sensitized RB acceptor emission is somewhat shortened with all the three architectures, only Yb@Er sample demonstrates tiny difference in the observed Er^{3+} luminescence decay (Fig. 4 d-f, Table S5), while in the other architectures the difference remains negligible. Due to the observed significant relative intensity and shortened luminescence decay of the sensitized RB acceptor emission, however, the results cannot be explained simply by assuming that a negligible fraction of Er^{3+} donor ions is involved in the RET and/or that the efficiency of RET is too weak to produce any significant change in the luminescence decay.

Nevertheless, strong RB emission in the steady-state luminescence spectra was acquired in Yb@YbEr samples. The relative RET sensitized RB acceptor emission was stronger in Yb@YbEr samples as compared to …@Er and Yb@Er and the I_{RB}/I_{Er} ratio increased in the order …@Er, Yb@Er and Yb@YbEr samples, most like due to higher recharging efficiency of Er^{3+} donors already deactivated upon RET. One should also note that for the Yb@YbEr sample with the 5% Er^{3+} doping, already the smallest RB concentration results in very high relative RET sensitized RB acceptor emission intensity (Fig. S9). We associate this with energy being channeled by continuous excitation and energy-migration (possibly via BET $Er^{3+} \rightarrow Yb^{3+}$ followed by $Yb^{3+} \rightarrow Yb^{3+}$ EM, or via also direct $Er^{3+} \rightarrow Er^{3+}$ EM) to those superficial $\boldsymbol{D_i}$ ions that are capable to RET or ET to $\boldsymbol{A}$. Thus, there would be $\boldsymbol{D_i}$ ions close to every RB even though very few RB molecules per particle is present. We should further consider the processes which are likely present in the system under consideration. In the course of the steady-state excitation, the $\boldsymbol{D_i}$ deactivated by RET can be rapidly recharged by the excited state energy of the Yb^{3+} ($\boldsymbol{S_i}$) network and the energy migration can be further facilitated by the continuous IR excitation and may result in that the $\boldsymbol{D_i}$ susceptible to RET are cycled, i.e. deactivated by RET and recharged, multiple times even during their normal luminescence lifetime. Further, energy migration through Yb^{3+} network together with possible back energy transfer from Er^{3+} donor ions to Yb^{3+} sensitizer facilitates efficient quenching (also the volumetric Er^{3+} ions) by e.g. water or ligands molecules surrounding the core only $NaYF_4$: Er^{3+},Yb^{3+} or the core-shell Yb@YbEr samples. This may also result in delayed channeling the excited state energy from the volumetric $\boldsymbol{S_i}$ and $\boldsymbol{D_i}$ ions to recharge the superficial $\boldsymbol{D_i}$ involved in efficient RET to $\boldsymbol{A}$. This would allow also the volumetric $\boldsymbol{S_i}$ and $\boldsymbol{D_i}$, which are beyond the Förster distance, to possibly indirectly participate to RET and also result in sensitized emission from surface-bound RB. The compositional architecture can thus play an unexpectedly important role in such steady-state luminescence RET response, and result in larger contribution to the sensitized acceptor emission intensity

than predicted by their relative concentration from the $\boldsymbol{D_i}$ within Förster distance of $\boldsymbol{A_j}$. This would, however, set additional challenges in modelling and analysis of the upconversion RET, together with the Förster radius being dependent on the $\boldsymbol{S_i}$ and $\boldsymbol{D_i}$ concentration and compositional architecture e.g. in the core@shell architecture. It is also obvious that the $\boldsymbol{D}$ emission decay kinetics alone cannot be used to confirm the RET mechanism, but the kinetics of the sensitized acceptor emission and also the rise part of the luminescence kinetics can be beneficial. The detailed understanding, how the sensitized $\boldsymbol{A}$ intensity response is increased by RET without significant apparent changes in the observed $\boldsymbol{D}$ emission kinetics, could be possible e.g. by extending the three-dimensional random walk model used for Monte Carlo simulation [58,59,61] of energy-migration processes in crystal lattice with core-shell structures and further including surface quenching effects and RET to surface-bound acceptors.

Considering the kinetic behavior of our samples in response to acceptor, the most significant (but still not large) change in Er^{3+} donor luminescence lifetime upon presence of the RB acceptor can be observed for Yb@Er sample (Fig. 4e and Table S5), despite steady-state spectra for this sample showed weakest intensity response (Fig 4l) in presence of the acceptor. On the other hand, for …@Er and Yb@YbEr samples (Fig. 4d and f) no significant changes in Er^{3+} donor luminescence lifetime are observed even the donor distribution within all the three architectures, in principle, is exactly the same. Generally, it would be expected that the donor luminescence decay of the samples should be shortened upon presence of acceptor, taking into account the fractions of Er^{3+} donor ions, which are susceptible to RET in each architecture. The lack of Er^{3+} donor luminescence decay changes would mean, that no or only a negligible fraction of Er^{3+} donor ions are participating to RET, but the sensitized RB acceptor emission with shortened decay should then have also a negligible intensity. The Yb@YbEr sample, which produced the strongest dependence on the RB acceptor concentration in the steady-state spectra, displays originally the shortest Er^{3+} luminescence lifetime due to parasite Yb^{3+} mediated surface

quenching in water, but it seems the RET can still compete efficiently with the surface quenching and thus lead to shortened decay of the sensitized RB acceptor emission, but again, without spectacular change in the Er^{3+} donor luminescence decay. Concluding, the donor luminescence lifetimes are only weakly sensitive to the RB presence, and similar observations can be found in some other research papers, where UCNPs were used as RET reporters[66]. It is also interesting to note the Yb@YbEr architecture shows bi-exponential decays (Table S5), which could be associated to two populations of Er^{3+} ions – the superficial ones that are highly susceptible to quenching (lifetime ~160 μs, whose contribution is 90% of the total Er^{3+} ions) and the one slightly deeper (with the lifetime of c.a. 700 μs with the contribution of ~10% of all Er^{3+} ions). The two other architectures, …@Er and Yb@YbEr, however, have in principle exactly the same distribution of Er^{3+}, but generally only a single Er^{3+} luminescence lifetime ~700 μs is found. Therefore, this biexponential decay of Er^{3+} luminescence must be a consequence of Yb^{3+} co-doping in the shell as the Yb^{3+} doping in the core alone (as in Yb@Er sample) does not result the same. It has been suggested that the observed Er^{3+} luminescence lifetimes and also the intrinsic QY of Er^{3+} are actually partly determined by the sensitization pathways and/or energy migration/cross-relaxation between the resonant Er^{3+} donor and Yb^{3+} sensitizer ions[50,64,103,104].

Based on steady state spectra (Fig.4a-c), RET efficiencies were estimated (Eq.S1) from the green 540 nm emission intensity of donor alone and donor in the presence of acceptor (Fig.4l, solid symbols). Despite high values are obtained, which monotonically respond to acceptor concentration, these quantitative numbers are most probably not exactly corresponding to RET efficiencies expected from molecular FRET theory. This is because the donor species (Er^{3+} ions) are continuously recharged by sensitizer ions (Yb^{3+} ions) even when the excitation pulse is finished, and thus we suspect it is risky to draw quantitative conclusions and derive the sensitivities. Importantly, the radiative reabsorption of donor NP emission by acceptor molecules at its surface cannot be unequivocally excluded with steady-

state detection approach. Moreover, the acceptor molecules on the surface of the NP in principle are experiencing the same 'constellation' configuration of the donor ions (i.e. namely the motif "…@Er" in present in all the three NP) against NP surface. Because the three samples differ in the compositional architecture of the Yb^{3+} sensitizer ions only, the observed differences, again, cannot be explained within the framework of conventional FRET theory. In the same time, the luminescence kinetics treated in conventional way (i.e. tail fitting) are much less sensitive (Fig.4l, open symbols), due to reasons discussed in this report. This clearly demonstrates the role of Yb^{3+} ions in energy storage, migration and recharging of donor Er^{3+} ions.

It has been also shown that the observed Er^{3+} upconversion luminescence decay is strongly dependent on the Yb^{3+} sensitizer concentration and that the decay is also affected by the Er^{3+} dopant concentration.[105] This can be due to changes in the excited-state lifetime of Yb^{3+} network, which is feeding the Er^{3+} upconversion by ETU. In case the intrinsic decay of $^2H_{11/2}$ or $^4S_{3/2}$ of Er^{3+} is faster than the ETU rate from Yb^{3+} ($^2F_{5/2}$) to Er^{3+}, the observed Er^{3+} upconversion luminescence decay would actually be determined by the decaying excited-state population of the Yb^{3+} in the network. Additionally, the deactivation by RET upon the surface bound RB acceptor would not be able to further shorten it. However, in addition to Yb^{3+} energy migration and ETU, one should expect $Er^{3+} \rightarrow Yb^{3+}$ back energy transfer and Er^{3+} - Er^{3+} cross-relaxation processes to be involved in Er^{3+} upconversion [50,64,103,104]. Together with the excited-state energy storage in the Yb^{3+} network ($^2F_{5/2}$), and also at intermediate excited state of Er^{3+} ions ($^4I_{11/2}$), piled during the wide-pulse excitation, these processes may cause delayed excitation, dynamic recharging and rebalancing of the excited-state distribution among the Er^{3+} ions and in consequence result in multi-step long distance energy migration in the Er^{3+} only, Yb^{3+} only, or Er^{3+}, Yb^{3+} co-doped matrixes. The observed Er^{3+} upconversion luminescence decay after the end of the

excitation pulse may thus be a combined effect of lifetime of the Yb^{3+} sensitizer network and above-mentioned rebalancing processes upon the energy stored at excited states, which is evidenced by smooth "delayed" start of the decays. Obviously, the rates of these different processes will depend on the Er^{3+} and Yb^{3+} dopant concentrations, and to study this further, steady-state and kinetic luminescence behavior of additional bunch of samples i.e. Yb@Yb, x%Er (x = 0.1%, 0.2%, 0.5%, 3%, 4%, 5%) were synthesized and experimentally studied titrating the RB acceptor and measuring both the donor and sensitized acceptor emission (Fig. S8). The kinetic studies made with short-pulse excitation revealed surprising strong dependence of the early part of the Er^{3+} luminescence decay after short-pulse excitation on the Er^{3+} concentration even when co-doped with 20% Yb^{3+}. With the lowest 0.1% Er^{3+} dopant concentration the delayed excitation was clearly observable indicating slower energy-exchange processes, but disappeared completely with the Er^{3+} dopant concentrations 3% or higher, which, on the other hand, showed the strongest response in the steady-state spectra to small RB acceptor concentrations. However, possibly due to the high rate of the energy-exchange reactions and the rapid decay of the Er^{3+} donor upconversion luminescence, the presence of the RB acceptor did not shorten the decay. The low 0.1% Er^{3+} dopant concentration was not sensitive to the small RB acceptor concentrations, but was the only sample which demonstrated a change in the Er^{3+} luminescence decay upon the higher RB acceptor concentrations.

Even though we have synthesized the UCNP architectures suggested by the VNP model based RET analysis, the experimental study revealed no significant improvement in the susceptibility of the Er^{3+} luminescence decay kinetics to the presence of RB acceptors. It is inevitable that due to the estimated Förster distance only a small fraction of the Er^{3+} donor ions can be directly involved in the RET even with full RB acceptor surface coverage. In the RET simulation and the initial analysis of the experimental data, we assumed that the Förster distance for RET between Er^{3+} and RB acceptor is constant

for different architectures. However, based on strong dependence of the observed luminescence decays on the Er^{3+} or Yb^{3+} dopant concentration, this is probably not true. Actually, the same value of intrinsic quantum yield for all the Er^{3+} donor ions in the three VNP architectures was assumed and nobody yet discussed that this quantity may vary for the individual Er^{3+} ions across the NP volume[23] and thus further complicate the analysis and affect the performance of the system, which by itself is already quite complex. Such conclusion is striking, but both the possible Er^{3+} to Yb^{3+} BET and Er^{3+} to Er^{3+} energy-exchange involving $^2H_{11/2}$ and $^4S_{3/2}$ would result in increased non-radiative relaxation of the emissive upconversion luminescence excited-state of the Er^{3+} and thus strongly decrease the Förster radius. Thus, the RET could have larger Förster distance in the compositions with low dopant concentrations (which are less bright and which have less superficial Er^{3+} donor ions) and oppositely, the Förster distances would be reduced in the compositions with higher Er^{3+} and/or Yb^{3+} ions (which would however be more bright). The 2% Er^{3+} may already be such a case, where the Förster distance is reduced from the expected around 2 nm, and thus only the extremely superficial Er^{3+} donor ions would be capable to efficiently RET to RB. But in the same time, these ions are also prone to competitive surface quenching, which may occur to be more efficient than RET itself. In consequence we hypothesize, the most effective Er^{3+} donor ions would be the ones in a very thin layer slightly below the surface. Namely, the very superficial donor ions are directly quenched, while those deeper in the shell participate in multiple ET processes and RET, but are more distant from the surface (or stay beyond Förster distance), and in consequence display reduced RET efficiency. Further, in case the non-radiative ET rates would be at best only slightly faster than the combined effect of other radiative or non-radiative relaxation pathways for the Er^{3+} donor, it could explain why we see only minor or negligible shortening of the Er^{3+} donor luminescence decay. On the other hand, in compositions with low concentrations of Er^{3+} and/or Yb^{3+}, where the energy migration is decreased, the larger Förster distance and longer original lifetime of the

Er^{3+} donor luminescence (owing to higher internal quantum yield) could favor observation of the shortened luminescence decay of Er^{3+} donor upon RET, but at the expense of the luminescence intensity. The improved energy migration and recharging of the Er^{3+} donor in compositions with high concentrations of Er^{3+} and/or Yb^{3+} ions may still improve the steady-state response in presence of the RB acceptor, but does not help in shortening the donor luminescence decay upon RET. This is because the Förster distance would be diminished and the Er^{3+} luminescence decay is already shorter due to the other non-radiative processes, and the effect of additional relaxation path (i.e. RET) would not anymore result in significant difference.

These conclusions would also mean that the same compositional architecture would not be able to concomitantly result in optimal performance of upconversion RET considering both steady-state luminescence intensity or in the luminescence decay responses. In particular, the improved energy migration will likely favor improved intensity response (at least in steady state measurement) but will reduces the change in the emission decay. Additionally, these results and discussion suggest the optimally responsive UCNPs as donors will not necessarily show the highest overall QY (and the resulting brightness). While the overall QY is easily manageable by surface passivation with a thick 3-5 nm undoped shell, the RET sensitivity becomes compromised in the same time, as the *D* and *A* species are concomitantly displaced by distance equal to the undoped shell thickness. The latter approach, unfavorably doubles or triples the donor acceptor distance and significantly reduces the RET sensitivity.

The Yb^{3+} sensitizer mediated surface quenching present in the Yb@YbEr architecture with co-doped shell, results in significantly shortened decay compared to the …@Er and Yb@Er architectures, and due to the additional non-radiative relaxation process this architecture should be considered as the worst candidate for RET. The steady-state luminescence behavior spectra (Fig. 4a-c), however, indi-

cates the opposite, because the Yb@YbEr compositional architecture results in the strongest RET response on donor intensity in presence of the RB acceptor and the highest relative sensitized RB acceptor emission. The different spectral responses obtained with the three samples upon presence of the RB acceptor gives evidence that the non-radiative RET mechanism must be involved as the reabsorption of the donor emission cannot fully explain the observations. This result obviously must indicate also that the distribution of Yb^{3+} sensitizer ions is important and has an impact on the RET response despite Yb^{3+} ions do not directly participate in RET[50,64,104]. The luminescence kinetics of the sensitized acceptor emission (590 nm) and donor emission in presence of surface bound acceptor (550 nm) show also differences compared to the donor only (550 nm) emission kinetics (Fig. 4 d-f).

Based on the luminescence rise- and decay-times (Tables S5-S7), we have calculated the RET efficiencies (Table S5, S6 and S7a). Due to inherent nature of up-conversion process, the luminescence lifetimes (typically used to quantify FRET efficiency) some luminescence risetimes are additionally observed which complicate the analysis. This is because the RET should be observed in the initial part of the luminescence decay, but this part of the kinetic profile is additionally affected by yet on-going process of building the population of emitting levels. Moreover, because the *D-A* luminescence lifetimes are often longer than the lifetime of the *D* alone, we hypothesize the RB molecules may additionally (especially at larger concentrations) mimic the protection layer of the nanoparticle against quenching by -OH vibrations. These results evidence how complex the analysis of the luminescence kinetics is in the case of UC-RET. We have therefore proposed to adopt another approach, where the disparities (Fig.4) are calculated and used as figure of merits in up-conversion RET assays analysis. To better visualize these differences in luminescence kinetics, we have defined acceptor ($\delta_{A/D} = I_A(t)@590 \,/\, I_D(t)@550$) and donor ($\delta_{DA/D} = I_{DA}(t)@550 \,/\, I_D(t)@550$) disparities as normalized ratios of their lu-

minescence kinetics compared to donor only luminescence. The non-radiative nature of the acceptor sensitization is supported by the more rapid rise of the sensitized RB acceptor emission at the start of the excitation pulse, and also by the accelerated decay of the sensitized RB acceptor emission upon end of the excitation pulse compared to the luminescence kinetics of the donor emission as shown in the acceptor disparity plots (Fig. 4 g-i). These changes in the luminescence kinetics are only possible if the ET mechanism contributing to the sensitized RB acceptor emission is non-radiative. It is however interesting to note that there are significant differences (especially in the donor disparity) between the different architectures.

Considering the changes in donor disparity (Fig. 4 g-i, dark grey) one may note the values of $\delta_{DA/D}$ are the largest for the Yb@Er sample. On the other hand, for the Yb@YbEr sample which gave the strongest steady state RET response, only tiny difference is observed in $\delta_{DA/D}$ when excitation pulse is switched off (Fig.4i at 2 ms) which suggests that the observed decay of D_i ions is not changed significantly upon participating to RET. Strangely, with ..@Er sample, significant values of $\delta_{DA/D}$ at the start of the excitation pulse can be observed, but absolutely no decrease can be noted when the excitation pulse is switched off. Actually with …@Er sample, the value of $\delta_{DA/D}$ slightly increases after the end of the excitation pulse, which may indicate that the donor luminescence lifetime was prolonged as a result of protection from solvent quenching by the of RB acceptor coordinated on the surface. It is thus obvious that the …@Er and Yb@YbEr samples are not suitable for conventional RET sensing based on luminescence decays. Interestingly, much larger differences exist in the risetimes of these samples, i.e. the steady state intensity is achieved faster for ***D-A*** as compared to ***D*** only case as a result of new non-radiative deactivation pathway present upon RET. This observation indicates new possibility to study RET in UCNPs donors by including the analysis of the luminescence rise kinetics during the excitation cycle using wide pulse excitation. The minimal or weak change of the luminescence

decay kinetics, however, cannot be solely explained by the minor fraction of total Er^{3+} ions participating in RET or weak energy-transfer efficiency, but must be related to the energy-migration processes involved. Concluding, the mechanism of the energy-transfer, and the explanation of the differences in the steady-state and kinetic luminescence response between the architectures, are not straightforward to decipher. The control experiments (Fig. S10), i.e. blocking the DNP surface with phosphate before mixing with RB acceptor to avoid surface attachment, however, verified the strong distance dependency of the observed sensitized RB emission. The contribution of the reabsorption based radiative energy-transfer clearly plays an unimportant role to the overall sensitized RB acceptor emission at dye concentrations employed for the full acceptor surface coverage and non-radiative RET must be involved even the Er^{3+} luminescence decays are not shortened as expected.

In the view of the presented discussion, the dynamic dopant-concentration dependent energy-exchange processes within the Er^{3+} and Yb^{3+} ions render it hard to make conclusions on the RET efficiency based solely on the changes in the luminescence decays. However, we discovered the early part of the luminescence rise curve could be an alternative tool to study the effect of the new non-radiative relaxation path provided by the surface attached RB acceptors. The rise time indicates how rapidly the equilibrium between the Er^{3+} donor excitation and the relaxation pathways is upon start of the wide-pulse excitation. In the presence of the attached RB acceptor, the RET should provide a new rapid non-radiative relaxation pathway to the excited-state of the Er^{3+} donors and result in that the equilibrium is achieved earlier. In the study of the luminescence kinetics, the rise part of the Er^{3+} donor luminescence kinetics with …@Er sample (Figure 4d, g and Table S6 and S7) showed shortening of the Er^{3+} donor luminescence rise time upon RET indicating that the steady-state equilibrium is achieved at lower excited-state concentration and thus more rapidly due to the new non-radiative relaxation process. With the Yb@Er sample (Figure 4e, h), however, the Er^{3+} donor luminescence rise time is prolonged upon

the presence of the RB acceptor even though the RET sensitized acceptor emission again rises more rapidly (Fig. 4 g-j). The possible explanation could originate from the slow energy-migration from the Yb^{3+} doped core through the Er^{3+} doped shell towards the surface of DNP. This would increase the time needed to reach the equilibrium in presence of the RB acceptor. The slow energy-migration process might be the reason why also the Er^{3+} donor emission decay is slightly affected upon the presence of the acceptor. In the Yb@YbEr sample, the shell is also co-doped with 20% Yb^{3+} and the energy-migration through the shell must be relatively rapid, and thus the RET to the surface bound RB acceptor is not fast enough to significantly decrease the excited-state concentration at which the equilibrium is achieved.

We have studied here the Yb-Er co-doped nanoparticles, but we believe part of the conclusions and work made here should be also valid for the other upconverting pairs. When the Yb is used as sensitizer, the Yb-Yb energy migration is present, and thus the conclusions related to the effect of energy-migration or recharging the donor ions are likely to be transferred to other activators as well. But due to specific differences in energy transfer (ET) rates, energy mismatches, back energy (BET) transfer efficiency, multi-phonon relaxations (MPR) etc. found in different activator (Tm, Ho, Eu, Tb donor ions), all these systems should be studied separately. For example, Tm-Tm ET rate (it results in concentration quenching) is significantly higher at the same distances and thus using these ions would therefore require ca. 0.2%Tm (ca. 10-time less than in Yb-Er case). In consequence, this purposefully reduced concentration of dopant would decrease number of donor ions available to acceptor molecules on the surface of nanoparticles. Ho^{3+} are similar but slightly dimmer than the Er^{3+} ions, but these ions have also demonstrated strong variation of spectral and temporal behavior in response to the architecture changes [78,106]. The upconversion in Eu or Tb ions is known[79,107], and the energy gaps in these

ions are beneficially large, making these ions resistant to non-radiative multiphonon relaxation or concentration quenching, but cooperative energy transfer (CET) found in Yb-Eu/Tb is ca. 100-fold weaker than ETU [108]. The core-multi-shell nanoparticles may additionally bring new knowledge and designs of RET donor nanoparticles. For example, by combining the up-conversion (YbTm at 980 nm) to Gd^{3+} ions, energy migration through intermediate Gd^{3+} doped shell aiming to excite Tb^{3+} or Eu^{3+} donor ions in the outermost shell. Such multi-shell approach and energy migration through Gd^{3+} ions could thus limit back energy transfer (Tb/Eu → Tm) which otherwise is known to compromise the brightness in homogenously co-doped materials. Definitely, a toolbox of energy transfer processes known in long-living levels in various lanthanide ions (ETU,CET,EM, CR etc.) combined with multi-shell approach and theoretical modelling, will enable to develop further new compositional architectures optimized to satisfy stringent requirements of the RET applications.

4. CONCLUSIONS AND OUTLOOK

In summary, we have simulated and experimentally studied the impact of different core-shell compositional architectures of UCNPs on the efficiency of resonance energy transfer to the surface bound acceptors and the kinetic and spectral response of such RET system. We first developed Virtual Nanoparticle Model (VNP) to *in-silico* calculate distribution of donors within the VNP and concentration dependent surface coverage of acceptor molecules on the VNPs, which enabled to study the statistics of closest $\boldsymbol{D_i}$-$\boldsymbol{A_j}$ pairs, and simulate the donor luminescence kinetics and intensity for various nanoparticle architectures versus the acceptor surface coverage, i.e. acceptor concentration. Small, medium and large core-only (20Yb2Er), active-core-undoped-shell (20Yb2Er@...), sensitized-core-active-shell (20Yb@20Yb2Er) and sensitized-core-active-shell with increased activator concentration

(20Yb@20YbXEr) were evaluated. By calculating acceptor concentration dependent donor-acceptor distance histograms, we managed to simulate luminescence lifetimes as well as expected luminescence intensities and ultimately propose an optimized NP architecture that should support the enhanced FRET sensing in upconversion mode. Next, these theoretical predictions let us synthesize corresponding core-shell nanoparticles, in order to perform FRET experiments with Rose Bengal acceptor molecules. These experimental studies further revealed that despite evident sensitized acceptor emission upon non-radiative energy-transfer, the donor luminescence lifetimes were not shortened as expected, indicating the importance of the spatial distribution of activator (donor) and sensitizer ions against acceptor molecules on the surface as well as the proportion of the effective donor ions to the total number of activator for sensitive UC-FRET. Moreover, the significant role and contribution of the other processes, such as the energy migration through sensitizer network and re-charging of the excited states of the donors involved in RET, were discovered, discussed and highlighted for the first time aiming to supplement the understanding of UCNP-RET.

Another important conclusion is related to the way FRET with UCNPs is quantified. Conventionally, the luminescence decay of $\boldsymbol{D}$ is used, but in case of UCNPs the long-range excitation energy migration in the sensitizer-activator (donor ions) network can render the change in luminescence decay negligible despite efficient RET (observed in steady-state spectra) would be present between superficial $\boldsymbol{D_i}$ and surface-bound $\boldsymbol{A_j}$. Our work shows that the intentional changes in the compositional architecture of UCNPs, achieved by designing dopant (i.e. activators and sensitizers) distribution in the donor nanoparticles, can provide improvements in the steady-state energy-transfer efficiency and intensity response to surface-bound acceptors, even if the changes in the luminescence decay are limited. Furthermore, we demonstrated, that despite the lack of significant change in the donor luminescence decay,

the energy transfer is mainly non-radiative. We have also pointed out that the intrinsic QY of the individual donor ions (that is required to evaluate individual $\boldsymbol{D_i}$ - $\boldsymbol{A_j}$ Förster distances) must also depend on numerous internal processes such as CR, BET and EM which in turn depend on the donor and co-doped sensitizer ion concentrations and spatial distribution. Such approach shows unprecedented perspective which must be considered to further optimize the compositional architecture of future UCNPs for UC-RET based sensing.

Despite complicated photoluminescent behavior of UCNP donors in RET, their high photostability, near-infrared excitation and anti-Stokes shifted emission enable to eliminate the autofluorescence background and can provide a route to unprecedented sensitivity in luminescence energy-transfer assays *in vitro* and sensors applicable *in vivo*, even with the optically most challenging clinically important matrices.

ASSOCIATED CONTENT

Supporting Information. Experimental details related to the design of VNP model, FRET mechanisms details, Förster distance calculation, synthesis of core-shell nanoparticles, X-ray diffraction and TEM data, steady-state and luminescence kinetics measurements for all samples.

Acknowledgements

A.P.-W. and A.M.K. contributed equally to this work. S.L. and T.S. acknowledge Business Finland for the financial support. A.K. acknowledges financial support from the National Science Centre Poland (Grant No 2021/41/N/ST5/02753). Calculations have been carried out using resources provided by Wroclaw Centre for Networking and Supercomputing (https://wcss.pl), grant No. 529.

[1] T. Forster, *Die Naturwissenschaften* **1946**, *33*, 166.

[2] I. Medintz, N. Hildebrandt, *FRET – Förster Resonance Energy Transfer*, Wiley-VCH Verlag GmbH & Co. KGaA, **2014**.

[3] J.-C. G. Bünzli, *Journal of Luminescence* **2016**, *170*, 866.

[4] N. Sirkka, A. Lyytikäinen, T. Savukoski, T. Soukka, *Analytica Chimica Acta* **2016**, *925*, 82.

[5] B. Wu, Z. Cao, Q. Zhang, G. Wang, *Sensors and Actuators B: Chemical* **2018**, *255*, 2853.

[6] L.-H. Yang, D. J. Ahn, E. Koo, *Materials Science and Engineering: C* **2016**, *69*, 625.

[7] P. Zeng, P. Hou, C. J. Jing, C. Z. Huang, *Talanta* **2018**, *185*, 118.

[8] T. Heyduk, *Current Opinion in Biotechnology* **2002**, *13*, 292.

[9] I. Iijima, M. Sisido, R. Abe, C. Komiyama, T. Hohsaka, D. Kajihara, *Nature Methods* **2006**, *3*, 923.

[10] A. Valanne, J. Suojanen, J. Peltonen, T. Soukka, P. Hänninen, H. Härmä, *Analyst* **2009**, *134*, 980.

[11] W. R. Algar, N. Hildebrandt, S. S. Vogel, I. L. Medintz, *Nature Methods* **2019**, *16*, 815.

[12] X. Qiu, N. Hildebrandt, *Expert Review of Molecular Diagnostics* **2019**, *19*, 767.

[13] G. Vereb, E. Jares-Erijman, P. R. Selvin, T. M. Jovin, *Biophysical Journal* **1998**, *74*, 2210.

[14] Y. Zhang, G. Wang, L. Yang, F. Wang, A. Liu, *Coordination Chemistry Reviews* **2018**, *370*, 1.

[15] E. Hemmer, P. Acosta-Mora, J. Méndez-Ramos, S. Fischer, *Journal of Materials Chemistry B* **2017**, *5*, 4365.

[16] D. Geißler, S. Linden, K. Liermann, K. D. Wegner, L. J. Charbonnière, N. Hildebrandt, *Inorganic Chemistry* **2014**, *53*, 1824.

[17] D. Casanova, D. Giaume, T. Gacoin, J.-P. Boilot, A. Alexandrou, *The Journal of Physical Chemistry B* **2006**, *110*, 19264.

[18] J. M. Zwier, N. Hildebrandt, Springer, Cham, **2017**, pp. 17–43.

[19] T. Soukka, T. Rantanen, K. Kuningas, *Annals of the New York Academy of Sciences* **2008**, *1130*, 188.

[20] R. Arppe, L. Mattsson, K. Korpi, S. Blom, Q. Wang, T. Riuttamäki, T. Soukka, *No Title*, American Chemical Society, **2015**.

[21] Y. Wang, K. Liu, X. Liu, K. Dohnalová, T. Gregorkiewicz, X. Kong, M. C. G. Aalders, W. J. Buma, H. Zhang, *Journal of Physical Chemistry Letters* **2011**, *2*, 2083.

[22] C. D. Laboda, C. L. Dwyer, *Advanced Functional Materials* **2016**, *26*, 2866.

[23] S. Bhuckory, E. Hemmer, Y.-T. Wu, A. Yahia-Ammar, F. Vetrone, N. Hildebrandt, *European Journal of Inorganic Chemistry* **2017**, *2017*, 5186.

[24] Y. Ding, F. Wu, Y. Zhang, X. Liu, E. M. L. D. De Jong, T. Gregorkiewicz, X. Hong, Y. Liu, M. C. G. Aalders, W. J. Buma, H. Zhang, *Journal of Physical Chemistry Letters* **2015**, *6*, 2518.

[25] A. L. De Guereñu, P. Bastian, P. Wessig, L. John, M. U. Kumke, *Biosensors* **2019**, *9*, 9.

[26] L. Francés-Soriano, N. Peruffo, M. M. Natile, N. Hildebrandt, *The Analyst* **2020**, *145*, 2543.

[27] S. Melle, O. G. Calderón, M. Laurenti, D. Mendez-Gonzalez, A. Egatz-Gomez, E. Lopez-Cabarcos, E. Cabrera-Granado, E. Diaz, J. Rubio-Retama, *Journal of Physical Chemistry C* **2018**, 4.

[28] A. P. Litvin, P. S. Parfenov, E. V. Ushakova, T. A. Vorsina, A. L. Simões Gamboa, A. V. Fedorov, A. V. Baranov, *Journal of Physical Chemistry C* **2015**, *119*, 17016.

[29] F. Zhang, C.-L. Zhang, W.-N. Wang, H.-P. Cong, H.-S. Qian, *ChemSusChem* **2016**, *9*, 1449.

[30] Y. Wang, B. Si, S. Lu, E. Liu, X. Hu, J. Fan, *Sensors and Actuators B: Chemical* **2017**, *246*, 127.

[31] H. Liu, J. Han, C. McBean, C. S. Lewis, P. Kumar Routh, M. Cotlet, S. S. Wong, *Physical Chemistry Chemical Physics* **2017**, *19*, 2153.

[32] S. Cui, S. Xu, H. Song, W. Xu, X. Chen, D. Zhou, Z. Yin, W. Han, *RSC Advances* **2015**, *5*, 99099.

[33] R. Marin, L. Labrador-Paéz, A. Skripka, P. Haro-González, A. Benayas, P. Canton, D. Jaque, F. Vetrone, L. Labrador-Pae, A. Skripka, P. Haro-Gonzaíez, A. Benayas, P. Canton, D. Jaque, F. Vetrone, L. Labrador-Paéz, A. Skripka, P. Haro-González, A. Benayas, P. Canton, D. Jaque, F. Vetrone, *ACS Photonics* **2018**, *5*, 2261.

[34] W. R. Algar, H. Kim, I. L. Medintz, N. Hildebrandt, *Coordination Chemistry Reviews* **2014**, *263–264*, 65.

[35] L. Mattsson, K. D. Wegner, N. Hildebrandt, T. Soukka, *RSC Advances* **2015**, *5*, 13270.

[36] Y.-W. Li, L. Dong, C.-X. Huang, Y.-C. Guo, X.-Z. Yang, Y.-J. Xu, H.-S. Qian, *RSC Advances* **2016**, *6*, 54241.

[37] S. Lahtinen, Q. Wang, T. Soukka, *Analytical Chemistry* **2016**, *88*, 653.

[38] J. Wang, R. Deng, *Chemistry - An Asian Journal* **2018**, *13*, 614.

[39] Z. Li, H. Yuan, W. Yuan, Q. Su, F. Li, *Coordination Chemistry Reviews* **2018**, *354*, 155.

[40] L. Labrador-Páez, D. J. Jovanović, M. I. Marqués, K. Smits, S. D. Dolić, F. Jaque, H. E. Stanley, M. D. Dramićanin, J. García-Solé, P. Haro-González, D. Jaque, *Small* **2017**, *13*, 1.

[41] W.-N. Wang, C.-X. Huang, C.-Y. Zhang, M.-L. Zhao, J. Zhang, H.-J. Chen, Z.-B. Zha, T. Zhao, H.-S. Qian, *Applied Catalysis B: Environmental* **2018**, *224*, 854.

[42] X. Guo, C. Chen, D. Zhang, C. P. Tripp, S. Yin, W. Qin, *RSC Advances* **2016**, *6*, 8127.

[43] X. Guo, W. Di, C. Chen, C. Liu, X. Wang, W. Qin, *Dalton Trans.* **2014**, *43*, 1048.

[44] J. Hu, S. Zhan, X. Wu, S. Hu, S. Wu, Y. Liu, *RSC Advances* **2018**, *8*, 21505.

[45] Y. Wang, B. Si, S. Lu, E. Liu, X. Hu, J. Fan, *Sensors and Actuators B: Chemical* **2017**, *246*, 127.

[46] S. M. Tawfik, H. H. Cho, B. T. Huy, T.-T. T. Nguyen, G. Zayakhuu, Y.-I. Lee, *Arabian Journal of Chemistry* **2018**, DOI 10.1016/j.arabjc.2018.06.019.

[47] Y. Zhang, S. Xu, X. Li, J. Zhang, J. Sun, L. Tong, H. Zhong, H. Xia, R. Hua, B. Chen, *Sensors and Actuators, B: Chemical* **2018**, *257*, 829.

[48] S. Hu, Y. Yu, X. Wu, P. Hu, H. Cao, Q. Wu, Z. Tang, Y. Guo, Y. Liu, *Journal of Rare Earths* **2017**, *35*, 120.

[49] Th. Förster, *Annalen der Physik* **1948**, *437*, 55.

[50] Z. Wang, A. Meijerink, *Journal of Physical Chemistry C* **2018**, *122*, 26298.

[51] B. Chen, F. Wang, *Accounts of Chemical Research* **2020**, *53*, 358.

[52] C. Ma, X. Xu, F. Wang, Z. Zhou, D. Liu, J. Zhao, M. Guan, C. I. Lang, D. Jin, *Nano Letters* **2017**, *17*, 2858.

[53] N. J. J. J. Johnson, S. He, S. Diao, E. M. Chan, H. Dai, A. Almutairi, N. J. J. J. Johnson, A. Almutairi, E. M. Chan, S. He, S. Diao, E. M. Chan, H. Dai, A. Almutairi, *Journal of the American Chemical Society* **2017**, *139*, 3275.

[54] L. Sun, R. Gao, T. Pan, X.-C. Ai, L. Fu, J.-P. Zhang, *No Title*, The Royal Society Of Chemistry, **2019**.

[55] R. Marin, D. Jaque, A. Benayas, *Nanoscale Horizons* **2021**, *6*, 209.

[56] S. Mei, J. Zhou, H. T. Sun, Y. Cai, L. D. Sun, D. Jin, C. H. Yan, *Advanced Science* **2021**, *8*, 1.

[57] Q. Su, S. Han, X. Xie, H. Zhu, H. Chen, C.-K. K. Chen, R.-S. S. Liu, X. Chen, F. Wang, X. Liu, *Journal of the American Chemical Society* **2012**, *134*, 20849.

[58] G. Ledoux, D. Amans, M.-F. F. Joubert, B. Mahler, S. Mishra, S. Daniele, C. Dujardin, *Journal of Physical Chemistry C* **2018**, *122*, 888.

[59] L. Tu, X. Liu, F. Wu, H. Zhang, *Chemical Society Reviews* **2015**, *44*, 1331.

[60] F. Wang, R. Deng, J. Wang, Q. Wang, Y. Han, H. Zhu, X. Chen, X. Liu, *Nature Materials* **2011**, *10*, 968.

[61] J. Zuo, D. Sun, L. Tu, Y. Wu, Y. Cao, B. Xue, Y. Zhang, Y. Chang, X. Liu, X. Kong, W. J. Buma, E. J. Meijer, H. Zhang, *Angewandte Chemie - International Edition* **2018**, *57*, 3054.

[62] R. Deng, J. Wang, R. Chen, W. Huang, X. Liu, *Journal of the American Chemical Society* **2016**, *138*, 15972.

[63] Y. Feng, Z. Li, Q. Li, J. Yuan, L. Tu, L. Ning, H. Zhang, *Light: Science & Applications* **2021**, *10*, 105.

[64] F. T. Rabouw, P. T. Prins, P. Villanueva-Delgado, M. Castelijns, R. G. Geitenbeek, A. Meijerink, *ACS Nano* **2018**, *12*, 4812.

[65] A. Teitelboim, B. Tian, D. J. Garfield, A. Fernandez-Bravo, A. C. Gotlin, P. J. Schuck, B. E. Cohen, E. M. Chan, A. Fernandez Bravo, A. C. Gotlin, J. Schuck, B. E. Cohen, E. M. Chan, A. Fernandez-Bravo, A. C. Gotlin, P. J. Schuck, B. E. Cohen, E. M. Chan, *Journal of Physical Chemistry C* **2019**, *123*, 2678.

[66] S. Melle, O. G. Calderóncalderón, M. Laurenti, D. Mendez-Gonzalez, A. Egatz-Gómezgómez, E. Lópezlópez-Cabarcos, E. Cabrera-Granado, E. Díaz, J. Rubio-Retama, *J. Phys. Chem. C* **2018**, *122*, 40.

[67] T. Riuttamäki, I. Hyppänen, J. Kankare, T. Soukka, *The Journal of Physical Chemistry C* **2011**, *115*, 17736.

[68] A. Das, C. Corbella Bagot, E. Rappeport, T. Ba Tis, W. Park, *Journal of Applied Physics* **2021**, *130*, 23102.

[69] C. Song, Z. Ye, G. Wang, J. Yuan, Y. Guan, *ACS Nano* **2010**, *4*, 5389.

[70] C. Siefe, R. D. Mehlenbacher, C. S. Peng, Y. Zhang, S. Fischer, A. Lay, C. A. McLellan, A. P. Alivisatos, S. Chu, J. A. Dionne, *Journal of the American Chemical Society* **2019**, *141*, 16997.

[71] L. Marciniak, A. Pilch, S. Arabasz, D. Jin, A. Bednarkiewicz, *Nanoscale* **2017**, *9*, 8288.

[72] L. Marciniak, K. Prorok, L. Francés-Soriano, J. Pérez-Prieto, A. Bednarkiewicz, *Nanoscale* **2016**, *8*, 5037.

[73] T. Wang, H. Zhou, Z. Yu, G. Zhou, J. Zhou, D. Huang, L. Sun, P. Gao, Y. Sun, J. Hu, *Journal of Physical Chemistry C* **2018**, *122*, 10113.

[74] Y. Zhang, J. Zhang, J. Sun, H. Xia, R. Hua, B. Chen, J. Beik, Z. Abed, F. S. Ghoreishi, S. Hosseini-Nami, S. Mehrzadi, A. Shakeri-Zadeh, S. K. Kamrava, L. R. Hirsch, N. J. Halas, J. D. Payne, *Optical Materials Express, Vol. 8, Issue 2, pp. 368-384* **2018**, *8*, 368.

[75] W. Schärtl, *Nanoscale* **2010**, *2*, 829.

[76] X. Wu, Y. Zhang, K. Takle, O. Bilsel, Z. Li, H. Lee, Z. Zhang, D. Li, W. Fan, C. Duan, E. M. Chan, C. Lois, Y. Xiang, G. Han, *ACS Nano* **2016**, *10*, 1060.

[77] W. Shao, G. Chen, T. Y. Ohulchanskyy, A. Kuzmin, J. Damasco, H. Qiu, C. Yang, H. Ågren, P. N. Prasad, W. Shao, G. Chen, H. Qiu, C. Yang, T. Y. Ohulchanskyy, A. Kuzmin, J. Damasco, P. N. Prasad, H. Ågren, *Advanced Optical Materials* **2015**, *3*, 575.

[78] A. Pilch, C. Würth, M. Kaiser, D. Wawrzyńczyk, M. Kurnatowska, S. Arabasz, K. Prorok, M. Samoć, W. Strek, U. Resch-Genger, A. Bednarkiewicz, *Small* **2017**, *13*, 54.

[79] K. Prorok, A. Bednarkiewicz, B. Cichy, A. Gnach, M. Misiak, M. Sobczyk, W. Strek, *Nanoscale* **2014**, *6*, 1855.

[80] D. Tu, L. Liu, Q. Ju, Y. Liu, H. Zhu, R. Li, X. Chen, *Angewandte Chemie - International Edition* **2011**, *50*, 6306.

[81] J. Zhang, B. Li, L. Zhang, H. Jiang, *Chemical Communications* **2012**, *48*, 4860.

[82] S. Xu, S. Xu, Y. Zhu, W. Xu, P. Zhou, C. Zhou, B. Dong, H. Song, *Nanoscale* **2014**, *6*, 12573.

[83] R. Chen, V. D. Ta, F. Xiao, Q. Zhang, H. Sun, *Small* **2013**, *9*, 1052.

[84] K. Smolarek, B. Ebenhoch, N. Czechowski, A. Prymaczek, M. Twardowska, I. D. W. Samuel, S. Mackowski, *Applied Physics Letters* **2013**, *103*, 203302.

[85] F. Gonell, M. Haro, R. S. Sánchez, P. Negro, I. Mora-Seró, J. Bisquert, B. Julián-López, S. Gimenez, *The Journal of Physical Chemistry C* **2014**, *118*, 11279.

[86] T. Li, Z. Wu, T. Huang, J. Liu, L. Rong, S. Lan, Z. Guo, H. Zhang, B. Yang, *RSC Advances* **2015**, *5*, 48024.

[87] L. Francés-Soriano, M. Liras, A. Kowalczyk, A. Bednarkiewicz, M. González-Béjar, J. Pérez-Prieto, *Nanoscale* **2016**, *8*, 204.

[88] X. Zhang, W. Chen, X. Xie, Y. Li, D. Chen, Z. Chao, C. Liu, H. Ma, Y. Liu, H. Ju, *Angewandte Chemie International Edition* **2019**, *58*, 12117.

[89] D. Wawrzynczyk, M. Nyk, A. Bednarkiewicz, W. Strek, M. Samoc, *Journal of Luminescence* **2013**, *133*, 138.

[90] S.-L. Lin, H.-C. Chen, C. A. Chang, *Nanomaterials* **2020**, *10*, 2035.

[91] D. Kang, S. Lee, H. Shin, J. Pyun, J. Lee, *Biosensors and Bioelectronics* **2020**, *150*, 111921.

[92] H. Ren, Z. Long, X. Shen, Y. Zhang, J. Sun, J. Ouyang, N. Na, *ACS Applied Materials & Interfaces* **2018**, *10*, 25621.

[93] A. Bednarkiewicz, E. M. Chan, K. Prorok, *Nanoscale Advances* **2020**, *2*, 4863.

[94] L. Marciniak, A. Pilch, S. Arabasz, D. Jin, A. Bednarkiewicz, *Nanoscale* **2017**, *9*, 8288.

[95] J. Zhou, C. Li, D. Li, X. Liu, Z. Mu, W. Gao, J. Qiu, R. Deng, *Nature Communications* **2020**, *11*, DOI 10.1038/s41467-020-18223-z.

[96] A. Bednarkiewicz, M. Nyk, M. Samoc, W. Strek, *Journal of Physical Chemistry C* **2010**, *114*, DOI 10.1021/jp106120d.

[97] V. Muhr, C. Würth, M. Kraft, M. Buchner, A. J. Baeumner, U. Resch-Genger, T. Hirsch, *Analytical Chemistry* **2017**, *89*, 4868.

[98] C. Meyer, M. Haase, W. Hoheisel, K. Bohmann, *CORE/SHELL NANOPARTICLES SUITABLE FOR (F)RET-ASSAYS*, **2004**.

[99] C. Würth, S. Fischer, B. Grauel, A. P. Alivisatos, U. Resch-Genger, *Journal of the American Chemical Society* **2018**, *140*, 4922.

[100] F. Wang, J. Wang, X. Liu, *Angewandte Chemie - International Edition* **2010**, *49*, 7456.

[101] Q. Li, X. Li, L. Zhang, J. Zuo, Y. Zhang, X. Liu, L. Tu, B. Xue, Y. Chang, X. Kong, *Nanoscale* **2018**, *10*, 12356.

[102] M. Xue, C. Cao, X. Zhou, M. Xu, W. Feng, F. Li, *Inorganic Chemistry* **2019**, *58*, 14490.

[103] J. Bergstrand, Q. Liu, B. Huang, X. Peng, C. Würth, U. Resch-Genger, Q. Zhan, J. Widengren, H. Ågren, H. Liu, *Nanoscale* **2019**, *11*, 4959.

[104] S. Mei, J. Zhou, H. T. Sun, Y. Cai, L. D. Sun, D. Jin, C. H. Yan, *Advanced Science* **2021**, *8*, 1.

[105] M. Kaiser, C. Würth, M. Kraft, T. Soukka, U. Resch-Genger, *Nano Research* **2019**, *12*, 1871.

[106] A. Pilch-Wrobel, B. Czaban, D. Wawrzyńczyk, A. Bednarkiewicz, *Journal of Luminescence* **2018**, *198*, 482.

[107] K. Prorok, M. Pawlyta, W. Strek, A. Bednarkiewicz, *Chemistry of Materials* **2016**, *28*, DOI 10.1021/acs.chemmater.6b00353.

[108] F. Auzel, *Chemical Reviews* **2004**, *104*, 139.

AUTHOR INFORMATION

A.P-W.: 0000-0003-1991-4008

A.K.: 0000-0001-6335-9537

S.L.: 0000-0003-2816-7809

T.S.: 0000-0002-1144-6724

A.B.: 0000-0003-4113-0365

NOTES

The authors declare no conflict of interests.

ACKNOWLEDGMENT

Business Finland is acknowledged for the financial support.

ABBREVIATIONS

UC – upconversion, UCNP – up-converting nanoparticle, FRET – Förster resonance energy transfer, RET– resonance energy transfer, ET – energy transfer, D – donor, A – acceptor, Ln – lanthanide, LnNP – lanthanide doped nanoparticles, DNP – donor nanoparticle, NP –nanoparticles, VNP – virtual nanoparticle, R_C – core radius, L_S – shell thickness, RB – Rose Bengal, XRD – X-ray Powder Diffraction

REFERENCES

Use the "Insert Citation" button to add citations to this document.

SYNOPSIS TOC

Core-shell design and composition of lanthanide doped upconverting donor nanoparticles strongly affects the resonance energy transfer based acceptor sensitization.